International Journal of Nanomedicine

Dovepress
open access to scientific and medical research

Open Access Full Text Article

ORIGINAL RESEARCH

Amelioration of diabetic nephropathy using pomegranate peel extract-stabilized gold nanoparticles: assessment of NF-κB and Nrf2 signaling system

This article was published in the following Dove Medical Press journal:
International Journal of Nanomedicine

Krishnendu Manna[1,*]
Snehasis Mishra[1,*]
Moumita Saha[1]
Supratim Mahapatra[1]
Chirag Saha[1]
Govind Yenge[2]
Nilesh Gaikwad[2]
Ramkrishna Pal[2]
Dasharath Oulkar[3]
Kaushik Banerjee[3]
Krishna Das Saha[1]

[1]Cancer Biology and Inflammatory Disorder Division, Council of Scientific & Industrial Research–Indian Institute of Chemical Biology, Kolkata 700032, West Bengal, India; [2]Postharvest Technology Laboratory, Indian Council of Agricultural Research-National Research Centre on Pomegranate, Solapur 413255, Maharashtra, India; [3]National Referral Laboratory, Indian Council of Agricultural Research-National Research Centre for Grapes, Pune 412307, Maharashtra, India

*These authors contributed equally to this work

Correspondence: Krishna Das Saha
Cancer Biology and Inflammatory Disorder Division, Council of Scientific & Industrial Research–Indian Institute of Chemical Biology, 4, Raja Subodh Chandra Mullick Road, Kolkata 700032, West Bengal, India
Tel +91 33 2499 5810
Fax +91 33 2473 5197
Email krishna@iicb.res.in

Background: Diabetic nephropathy (DN), an end-stage renal disorder, has posed a menace to humankind globally, because of its complex nature and poorly understandable intricate mechanism. In recent times, functional foods as potential health benefits have been gaining attention of consumers and researchers alike. Rich in antioxidants, the peel and seed of pomegranate have previously demonstrated protection against oxidative-stress-related diseases, including cardiovascular disorders, diabetes, and cancer.

Purpose: This study was designed to investigate the ameliorative role of pomegranate peel extract–stabilized gold nanoparticle (PPE-AuNP) on streptozotocin (STZ)-induced DN in an experimental murine model.

Methods: Following the reduction methods, AuNP was prepared using the pomegranate peel ellagitannins and characterized by particle size, physical appearance, and morphological architecture. Modulatory potential of PPE-AuNP was examined through the plethora of biochemical and high throughput techniques, flow cytometry, immunoblotting, and immunofluorescence.

Results: The animals treated with PPE-AuNP markedly reduced the fasting blood glucose, renal toxicity indices, and serum TC and TG in a hyperglycemic condition. As evident from an increased level of plasma insulin level, PPE-AuNP normalized the STZ-induced pancreatic β-cell dysfunction. The STZ-mediated suppression of endogenous antioxidant response was restored by the PPE-AuNP treatment, which reduced the generation of LPO as well as iROS. Furthermore, the hyperglycemia-mediated augmentation of protein glycation, followed by the NOX4/p-47^{phox} activation, diminished with the application of PPE-AuNP. The histological and immunohistochemical findings showed the protective efficacy of PPE-AuNP in reducing STZ-induced glomerular sclerosis and renal fibrosis. In addition, it reduced proinflammatory burden through the modulation of the MAPK/NF-κB/STAT3/cytokine axis. Simultaneously, PI3K/AKT-guided Nrf2 activation was evident upon the PPE-AuNP application, which enhanced the antioxidant response and maintained hyperglycemic homeostasis.

Conclusion: The findings indicate that the use of PPE-AuNPs might act as an economic therapeutic remedy for alleviating DN.

Keywords: pomegranate polyphenol, gold nanoparticle, diabetic kidney disease, advanced glycation end-product, NF-κB, STAT3, Nrf2

Introduction

In recent years, diabetes mellitus (DM), also known as hyperglycemia, is a public health problem. As a continual metabolic ailment in which the body is unable to

submit your manuscript | www.dovepress.com
Dovepress
http://dx.doi.org/10.2147/IJN.S176013

utilize glucose for cellular energy, DM is either caused by insufficiency of insulin or resistance toward the insulin produced within the body.[1] Excessive hyperglycemia might lead to health complications such as diabetic nephropathy (DN), diabetic neuropathy, and diabetic retinopathy.[2] Among them, DN, the primary end-stage renal disease, accounts for significant morbidity and mortality.[3] A plethora of signaling abnormalities is associated with the disease progression that collectively results in the clinical and pathologic hallmarks of DN, namely progressive albuminuria, followed by a decline in glomerular filtration rate and kidney failure. This is simultaneously accompanied by podocyte loss, progressive glomerular sclerosis, and tubulointerstitial fibrosis.[3] Several lines of evidence suggested that hyperglycemia-associated metabolic and hemodynamic derangements activate signaling cascades.[4] Excessive blood glucose reacts with endogenous protein to produce advanced glycated end products (AGEs) and trigger the generation of reactive oxygen species (ROS) with a subsequent activation of protein kinase C-mediated transforming growth factor β-Smad-mitogen-activated protein kinase (TGF-β-Smad-MAPK). The downstream signaling response also mediates through Janus kinase (JAK) signal transducer and activator of transcription proteins (STAT), which further couples with the G protein signaling cascade.[4–6] The aberrant expression of cyclin kinases/extracellular matrix (ECM) proteins, metalloproteinase, and polyol pathways in addition to rennin-angiotensin system have been thought to be involved in the development and progression of DN.[6] An intricate crosstalk mechanism exists in these cellular signaling systems that accentuate hyperglycemia-induced complication and initiate other pathological processes associated with DN.[7] Also, an imbalance of redox-homeostasis triggers an overabundance of redox-regulated transcription factors, such as NF-κB, STAT3, and Nrf2, which are related to the modulation of hyperglycemia-induced renal inflammation.[8] A growing body of evidence suggests that ROS-mediated activation of the receptor for advanced glycated end products (RAGE) further turns on the molecular switch that is associated with the activation of NF-κB, which then causes renal inflammation.[9] On the contrary, Nrf2, another redox-sensitive transcription factor, is involved in the initiation of cellular defense mechanism and is known to play a protective role in DN, which could be a new choice for the treatment of DN.[10] As none of the drugs launched to date have demonstrated promising potential to cure DN, an efficient and restorative economic molecule is needed which can control hyperglycemia-induced oxidative stress, disquieting different cellular signaling pathways.

Earlier studies have indicated that the edible parts of certain medicinal plants possess beneficial effects upon renal functions in DM.[11–13] Since ages, pomegranate (*Punica granatum* L.) has been used for several medicinal purposes, particularly managing diarrheal, parasitic, and inflammatory disorders.[14] Pomegranate peel extract (PPE) contains a variety of polyphenolic compounds, including flavonoids, both condensed and hydrolyzable tannins, among others – all shows high antioxidant activity through free-radical-scavenging mechanism.[15] Enriched with antioxidants, the peel and seed of pomegranate have demonstrated protection against oxidative-stress-related diseases, including cardiovascular disorders, DM, and cancer.[14] Most of the plant bioactive molecules are inherently unstable in nature and are susceptible to spontaneous and enzymatic hydrolysis.[16] Despite numerous beneficial effects, the pomegranate peel has remained underutilized.

In the new millennium, nanoparticles of noble metals such as silver, gold, and platinum are used in a wide range of products including soaps, detergent, cosmetics, and toothpaste, along with medical and pharmaceutical applications. Due to the growing microbial resistance against metal ions and antibiotics and the development of resistant strains, the metallic nanoparticles are considered quite promising and therefore are emerging as a topic of interest to many researchers. The formulation of pomegranate polyphenols into biocompatible and biodegradable gold nanoparticles (AuNPs) could conquer the susceptibility to gastrointestinal hydrolysis of bioactive compounds and increase their absorption, stability (enhanced half-life), and systemic bioavailability.[17] For their ability to modulate the expression of cellular signaling molecules related to the inflammatory reactions, AuNP has garnered considerable attention of researchers in the past.[18] Previously published reports have demonstrated the non-toxic and protective effects of AuNP over the organs, without inducing any adverse effects in the rodent model, thereby having a continual control over the disease progression has remained indeterminate. Given the gap of knowledge, we aimed to evaluate the modulatory potential of PPE-AuNP on STZ-induced DN in mice while exploring the possible mechanism of action. A clear study over the mechanism and the downstream pathways through which the AuNP modulate the control over the antioxidant system to reverse the effect over diabetic conditions may solely contribute to its future therapeutic application in DM.

Materials and methods

Chemicals

All pure and analytical grade chemicals were purchased from Merck Millipore (Billerica, MA, USA). All analytical

standards were procured from Sigma-Aldrich Co. (St Louis, MO, USA). The other reagents of analytical grade were obtained from Sysco Research Laboratories (Mumbai, India). All antibodies used in the entire experimentation were obtained from Cell Signaling Technology (Danvers, MA, USA).

Plant material collection and preparation

Pomegranate fruits were collected from the garden of Indian Council of Agricultural Research-National Research Centre on Pomegranate (Solapur, India) in January 2017. The peels were separated, washed in an acetic acid solution (2%) for 1 hour, dried at 50°C for 24 h on a hot air plate, and ground to powder form.[19]

Preparation of PPE

The dried peel powder was extracted with 10% methanol under refluxing conditions and allowed to stand for overnight. After filtering and subsequent drying in a vacuum evaporator, the extract was suspended in 2% aqueous acetic acid before partitioning it with ethyl acetate. Thereafter, the ethyl acetate fractions were evaporated to dryness and dissolved in 10% methanol. Through 0.45 µm membrane, this solution was filtered and kept aside for the preparation of the AuNPs.

Liquid chromatography-mass spectrometry (UPLC-[ESI]-QToF-MS) conditions

An Acquity Ultra Performance Liquid Chromatograph (UPLC), coupled with a quadrupole-time of flight mass spectrometer (QToF-MS, Synapt G2 HDMS; Waters Corporation, Manchester, UK), was used with electrospray ionization (ESI). The mass resolution was set at 20,000 and the system was controlled by MassLynx 4.1 software. The method involved speedy swapping from low energy scan at 4 V (full scan mass spectrometry) to high energy scan at 10–60 V ramping during a single liquid chromatography run. The optimized instrument parameters included capillary voltage (3 kV), sampling cone (30 V), extraction cone (5 V), source temperature (120°C), desolvation temperature (500°C), desolvation gas flow (1,000 L/h), and cone gas flow (50 L/h). An Acquity UPLC BEH C18 column (2.1×100 mm, 1.8 µm; Waters India Pvt. Ltd., Bengaluru, India) was used, with the mobile phase comprising A: methanol:water (10:90, v/v) and B: methanol:water (90:10, v/v) with 0.1% formic acid in both phases. The flow rate was 0.4 mL/min. The chosen gradients were as follows: 90% A (0–0.5 minutes), 50% A (4.5 minutes), 50%–2% A (4.5–8 minutes), 2% A (8–11 minutes), 2%–90% A (11–11.5 minutes), and 90% A (12–15 minutes).[20]

Liquid chromatography-mass spectrometry data analysis

With reference to an in-house developed compound database (>1,200 compounds), the data processing was performed using the software UNIFI (version 1.7; Waters Corporation). For putative identification of the potential bioactive compounds, the mass error limit was set at 5 ppm. The compounds were relatively quantified against the certified reference standards of quercetin (for the non-anthocyanins) and pelargonidin-3-O-glucoside (for the anthocyanin derivatives).[20]

PPE-stabilized AuNP preparation

The gold ion solution was prepared by diluting 30% of tetrachloroaurate ($HAuCl_4$) in double distilled water to form a stock solution (0.01%). AuNP was prepared by adding this solution to PPE (10 mg/mL) drop by drop at 60°C while vigorously stirring. The formation of AuNP was confirmed within a few seconds with the change in color from gold to deep purple and eventually to wine red. Using a UV-Vis spectrophotometer (Shimadzu UV-1650) at 540 nm, the color intensity was measured.[21] The absorption spectra of the biosynthesized PPE-AuNPs were acquired in the wavelength ranging between 200 and 800 nm.[22]

Particle size analysis of PPE-AuNP using dynamic light scattering (DLS)

Particle size (hydrodynamic diameter) and size distribution measurements of the biosynthesized PPE-AuNP were carried out using Zetasizer, version 6.32 (Malvern Instruments, Malvern, UK), based on DLS.[23]

Fourier transform infrared (FTIR) spectroscopy

The FTIR spectroscopy measurements were carried out in order to identify and characterize the possible involvement of the functional groups of PPE in AuNP synthesis and stabilization. The FTIR spectra of PPE and dried biosynthesized AuNPs were acquired in an Avatar 330 FTIR spectrometer (Thermo Fisher Scientific, Waltham, MA, USA) over a range of 4,000–500 cm^{-1} after mixing with KBr pellets.[22]

Powder X-ray diffraction (XRD) study

The XRD patterns of the solid sample were recorded on a Bruker D8 ADVANCE SWAX diffractometer, which was operated at 40 kV and 40 mA. The instrument was calibrated with a standard silicon sample by Ni-filtered Cu Kα (λ=0.15406 nm) radiation.

Transmission electron microscopy (TEM)

The high resolution TEM (HR-TEM) images of PPE-AuNPs were observed using a JEOL 2010 TEM instrument (JEOL, Tokyo, Japan) operated at 200 kV. The sample for TEM analysis was prepared by dropping a sonicated ethanolic suspension of the sample onto the carbon-coated copper grid.

Atomic force microscopy (AFM)

In order to observe the surface morphology and measure the size of the resultant PPE-AuNP, an AFM was used. The sample was dropped onto freshly cleaved mica slices and dried overnight. An AGILENT-N9445A series 5500 AFM (Agilent Technologies, Santa Clara, CA, USA), which was equipped with PicoView software, was used.

Animals

Adult male BALB/c mice ranging from 8 to 10 weeks of age, with initial body weights of 20–22 g were procured from the inbred institutional facility. During the study, the animals were maintained under standard laboratory conditions of 21°C±2°C, relative humidity of 55%, and 12:12-hour of light:dark cycles. The animals were given standard rat pellets and tap water ad libitum. All experimental protocols were performed as per the guideline of the Institutional Animal Ethics Committee, Council of Scientific & Industrial Research–Indian Institute of Chemical Biology, and approved by the Committee for the Purpose of Control and Supervision of Experiments on Animals, Ministry of Environment, Forests and Climate Change, The Government of India.

Experimental design

The design of the overall experimentation is illustrated in Figure 1. Male mice were randomly divided into the following five groups, consisting of six mice in each group:

Group I

This group served as control. The mice in this group were kept at a standard ambient temperature of 24°C±2°C and 60%–70% relative humidity.

Group II

The mice in this group were treated with single intraperitoneal (IP) injection of streptozotocin (STZ) at a dose of 200 mg/kg body weight after dilution in citrate buffer solution (0.1 M, pH 4.5). The induction of diabetes was confirmed on the 7th day by checking the fasting glucose level (>200 mg/dL).

Groups III–V

PPE-AuNP was applied IP (5, 15, and 25 mg/kg body weight, respectively) on 5 alternate days (8th, 10th, 12th, 14th, and 16th) after the induction of diabetes.

In a separate set of experimentation, mice were treated with PPE in various concentration (5, 15, 25, and 100 mg/kg) for 5 alternate days (8th, 10th, 12th, 14th, and 16th) after STZ challenge to assess the efficacy of PPE alone over PPE-AuNP. At the completion of the experiment on the 18th day, each mouse was kept under fasting overnight, weighed, and sacrificed. After the blood sample was drawn through retro-orbital puncture, the serum and plasma samples were separated. The kidney sample was rapidly dissected out and weighed. The longitudinal section of the right kidney from each animal was used for the histopathological and immunohistochemical examinations. The renal cortices of the remnant kidney tissues were collected for assessing the other biochemical and molecular aspects. Single cells isolated from renal tissue were subjected to flow cytometric evaluation.

Determination of blood glucose

Blood glucose level (mg/dL) was determined based on the Glucose Oxidase Method.[24]

Determination of plasma insulin and HbA1C

Plasma insulin and glycated hemoglobin (HbA1C) were measured by using an ELISA kit (Aviva Systems Biology, San Diego, CA, USA) as per the manufacturer's instruction.

Estimation of renal toxicity marker

The renal toxicity indices, serum urea, and creatinine were estimated using a commercially available kit (Abcam, Cambridge, MA, USA) according to the manufacturer's protocol.

Estimation of serum total cholesterol (TC) and triglycerides (TGs)

The levels of TG and TC in serum were spectrophotometrically determined by using enzymatic colorimetric assay kits (Span Diagnostic Ltd., Mumbai, India).

Determination of renal intercellular reactive oxygen species (iROS)

The level of iROS was measured using the oxidation sensor dye 2′,7′-dichlorofluorescein diacetate (H_2DCFDA), wherein an increase in green fluorescence intensity is used to quantify the generation of intracellular ROS with respect

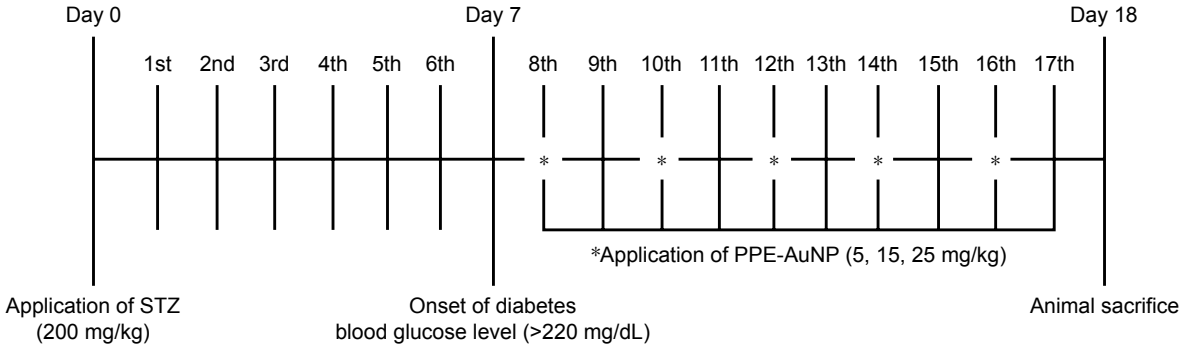

Figure 1 Schematic representation of experimental design outlining the phases of STZ-administration along with the PPE-AuNP application.
Abbreviations: PPE-AuNP, pomegranate peel extract-stabilized gold nanoparticle; STZ, streptozotocin.

to untreated control. The harvested renal cells (2×10^6) were resuspended in a complete medium containing H_2DCFDA and later incubated at 37°C for 30 minutes, following the acquisition by BD FACSAria III™ (Becton Dickinson, Franklin Lakes, NJ, USA) flow cytometer using an argon laser at 488 nm.[25]

Preparation of renal tissue homogenate

The renal tissues from the control and experimental groups of mice were excised, rinsed with ice-cold saline, and homogenized in 100 mM Tris–HCl buffer (pH 7.4) using a Teflon homogenizer. At 4°C, the tissues were centrifuged at 12,000×*g* for 30 minutes. The supernatant was separated and used for the biochemical estimations. In addition, the protein content in the tissue homogenate was also estimated.[26]

Determination of renal lipid peroxidation (LPO)

Renal LPO was determined by measuring the thiobarbituric acid reactive substance (TBARS) in the tissue lysate according to the standard protocol. Briefly, the cell lysate was incubated with 15% trichloroacetic acid (TCA), 0.375% thiobarbituric acid, and 5N hydrochloric acid (HCl) at 95°C for 15 minutes. The mixture was cooled and centrifuged, and the supernatant was collected. The absorbance of this supernatant was measured at 550 nm, and the results were calculated and expressed as nM of TBARS/mg protein against an appropriate blank.[27]

Determination of renal superoxide dismutase (SOD) activity

Using a commercially available kit (Sigma-Aldrich Co.), which underlies the protocol of WST-1 (highly water-soluble tetrazolium salt) reduction method according to the manufacturer's instruction, the activity of SOD was determined.

Determination of renal reduced glutathione (GSH) level

The tissue lysate was treated with 0.1 mL of TCA (25%), and the resulting precipitate was pelleted by centrifugation at 3,900×*g* for 10 minutes. The free endogenous sulfhydryl was assayed in the reagent-lysate mixture (3 mL), containing 2 mL of 0.5 mM 5,5′-dithiobis-2-nitrobenzoic acid (DTNB) with 1 mL of tissue lysate. The reduced GSH reacted with DTNB and formed a yellow colored complex. Finally the absorbance was measured at 412 nm.[28]

Determination of tissue nitrite (NO)

By using the Griess reagent containing 0.2% naphthylethylenediamine dihydrochloride, and sulfanilamide (2%) in phosphoric acid (5%), the tissue nitrite formation was determined. The Griess reagent (990 µL) was mixed with 10 µL of the cell lysate. After 5 minutes of incubation at 37°C in the dark, the absorbance was measured at 540 nm, and then, the value was calculated from the standard curve using sodium nitrite ($NaNO_2$, 1 mM).[29]

Determination of protein expression using flow cytometry

The quantification of intercellular protein expression was performed using flow cytometry through indirect immunofluorescence techniques. Briefly, the isolated renal cells were fixed in paraformaldehyde (4%) in PBS (pH 7.4) for 20 minutes at room temperature and permeabilized in Triton X-100 (0.1%) in PBS with FBS (0.1%) for 5 minutes. The permeabilized single cells were then incubated with the primary antibody (1:200) against AGE, RAGE, NOX4, p-p47^{phox}, p-PI3K, p-AKT, Keap1, and p-Nrf2 for 30 minutes at 4°C. After incubation, the cells were washed with PBS, followed by incubation for 30 minutes at 4°C in the presence of FITC/Alexa Fluor 647-conjugated anti-mouse/rabbit

IgG antibody. The stained cells were acquired using BD FACSAria III™ (Becton Dickinson). The resultant fluorescence intensity was analyzed through Flow Jo software. In each experiment, about 10,000 cells were analyzed.[27]

Determination of protein expression using immunofluorescence

The unstained renal section (6 µm of thickness) of all experimental groups was analyzed through indirect immunofluorescence.[27] Briefly, the sections were deparaffinized and hydrated in graded ethanol, followed by blocking (0.3% hydrogen peroxide) for 20 minutes to mask the endogenous peroxidase activity. A microwave oven was used to retrieve the antigen using citrate buffer (10 mM, pH 6.0) at temperatures ranging between 95°C and 98°C for 15 minutes, and then the section was further blocked with BSA (5%) for 30 minutes at 37°C. The sections were incubated with the primary antibody against TGF-β, Collagen IV, p65, Nrf2, Mn-SOD, and COX2 (dilution: 1:250) at 4°C for overnight. After washing the samples with PBS, the sections were incubated with anti-rabbit/mice-FITC/phycoerythrin (PE)/allophycocyanin (APC) secondary antibody for 1 hour each at 37°C, followed by nuclear staining with DAPI for 10 minutes. The images were observed in an Olympus FV1000 MPE SIM Laser Scanning confocal microscope (Olympus Corporation, Tokyo, Japan).[27,30] The resultant intensity was analyzed by using ImageJ software.

Determination of protein expression using immunoblotting

A renal tissue lysate was prepared using tissue lysis buffer containing Tris–HCl (20 mM) pH 7.5, 2-mercaptoethanol (50 mM), ethylene glycol-bis(β-aminoethyl ether)-N,N,N′,N′-tetraacetic acid (5 mM), EDTA (2 mM), NP40 (1%), SDS (0.1%), deoxycholic acid (0.5%), NaF (10 mM), phenylmethane sulfonyl fluoride (1 mM), leupeptin (25 mg/mL), and aprotinin (2 mg/mL), followed by the determination of protein concentrations using a protocol of Lowry et al. Protein fractions were reconstituted in a sample buffer, containing Tris–HCl (62 mM), SDS (2%), glycerol (10%), and β-mercaptoethanol (5%) and boiled at 97°C for 6 minutes for protein denaturation. Equal amounts (25 µg) of the denatured protein samples were separated using SDS-PAGE on a polyacrylamide gel (12.5%) and transferred overnight onto polyvinylidene difluoride membranes. The membranes were blocked with non-fat dried milk (5%) in Tris-buffered saline, containing Tween-20 (1%) for 1 hour at room temperature, followed by incubation of the respective primary antibodies (1:1,000 dilution) for overnight. The secondary antibody coupled with either alkaline phosphatase-conjugated goat anti-rabbit or anti-mouse antibodies (1:5,000) were used for a second incubation for 2 hours after washing with Tris-buffered saline, consisting of Tween-20 (1%). The blots were detected using a chromogenic substrate, nitro blue tetrazolium/5-bromo-4-chloro-3-indolyl-phosphate, and the photographs were taken using a Chemidoc XR Imager (Bio-Rad Laboratories Inc., Hercules, CA, USA).[31] The relative density of each blot was measured using ImageJ software.[27,32]

Determination of proinflammatory cytokine level

IL 1-beta (IL-1β), IL-2, IL-6, IL-10, and tumor necrosis factor-alpha (TNF-α) concentrations in the renal tissue samples were analyzed by using commercially available kits from eBiosciences (Santa Clara, CA, USA). Absorbance was measured at 450 nm.[30]

Biodistribution of PPE-AuNP using inductively coupled plasma mass spectrometry

To estimate the approximate concentration of PPE-AuNP in the kidney (0.1 g) and plasma (0.1 mL), the tissue was dissolved in the digestion solution containing nitric acid (HNO_3) and perchloric acid ($HClO_4$) of 5:1 ratio. Until the reaction equilibrium was attained, the solution was heated to 230°C–280°C. The digested tissue and plasma samples were used to determine the PPE-AuNP concentrations with inductively coupled plasma mass spectrometry.[33] The contents of PPE-AuNP in the renal tissue and plasma were calculated using the following equation:

$$\text{PPE-AuNP concentration } (\mu g/gm) = \frac{\text{Au in tissue suspension} \times 25}{\text{Wet weight of tissue}}.$$

Statistical analyses

All the values in the figures are expressed as mean values with their standard errors (mean ± standard error of mean [SEM]) of n observations, where n (n=5) represents the number of animals studied. In the experiments involving histology and immunohistochemistry, the figures shown are representative of at least three sections of the tissues collected from all the animals in each group. The information obtained from each group was statistically processed according to the most suitable technique for each case. A statistical software, OriginPro (version 8.0), was used for the data analysis, followed by the evaluation of the statistical significance using a one-way ANOVA through the Tukey method with the post hoc test. The critical significance level was set at $P<0.05$.

Results

Characterizations of PPE

A total of 17 phenolic compounds were putatively identified in PPE, namely (−) epigallocatechin gallate, 3′,4′,5,7-tetrahydroxyisoflavanone, 6″-O-acetyldaidzin, cyanidin 3-O-xyloside, dihydroquercetin 3-O-hexoside, ellagic acid, ellagic acid arabinoside, ellagic acid glucoside, epigallocatechin (−), gallagic acid, gallic acid, isopeonidin 3-O-sambubioside, kaempferol 3-(2G-rhamnosylrutinoside), kaempferol 3-O-rhamnoside, leucopelargonidin, methylgalangin, and punicalin (Table 1). Among them, ellagic acid and its derivatives were the most predominant compounds, having $[M–H]^-$ at m/z 303.01, 435.06, and 465.07 (Figure 2). With respect to the aqueous extract (25.24%), the total phenols in the peel extract was 2,893 mg/L of galic acid (GA) equivalent (mg/L), displaying the total phenolics of about 65%. The presence of 17 significant compounds suggested the basis of antioxidant and reducing properties of PPE.

Synthesis and characterization of PPE-AuNP

The total phenolic content of PPE reduced chloroauric acid at room temperature and pH 7.4 (Figure 3A). The color of the mixture was changed from pale gold/colorless to wine red in a span of 15 minutes, indicating the formation of the gold-conjugated PPE (PPE-AuNP). In this particular process of environmentally friendly synthesis of PPE-AuNPs, the gold particles interacted with PPE without involving any other artificial reagent. The stability of PPE-AuNP was evaluated in different time frames with regard to the change in colors (Figure 3B). The primary color (wine red) of the stabilized nanoparticles (PPE-AuNP) turned pink on the 30th day, following the final transformation to violet on the 60th day. This suggests the time-dependent aggregation at room temperature, which was later confirmed by using different high-throughput biophysical techniques. The spectrophotometric analysis of PPE-AuNP had an absorption maximum at 525 nm just after synthesis, and the intensity was gradually decreased with time (30th and 60th day) at room temperature (Figure 3C). The nanoparticles exhibited excellent stability at 4°C for 6 months and the absorption maxima remained almost unchanged over the span of 6 months, suggesting their temperature-dependent deformation. The DLS analysis of the nanoparticles showed PPE-AuNP having a hydrodynamic diameter of 20.4±0.347 nm at synthesis (0 day). However, a gradual increase in their size was noted with time (100.54±0.236 nm on the 30th day and 120.24±0.354 nm on the 60th day) (Figure 3I–K). The particle diameter of PPE-AuNP was also validated in AFM microscopy where a progressive aggregation tendency was found after the 30th and 60th day of storage at room temperature. On the day of synthesis, the electron micrographs also demonstrated aspherical nature of the PPE-AuNP, which gradually became flattened after 30 and 60 days of storage

Table 1 Characterization of phenolic compounds of PPE using LC-ESI/MS analysis

Component name	Expected mass (Da)	Observed m/z	Mass error (mDa)	Mass error (ppm)	Retention time (min)	Detector response	Adducts
(−) Epigallocatechin gallate	458.08	481.07	−0.91	−1.88	3.17	1,926.77	+Na, +H
3′,4′,5,7-Tetrahydroxyisoflavanone	288.06	289.07	0.73	2.51	3.60	1,129.09	+H
6″-O-Acetyldaidzin	458.12	459.12	−1.15	−2.49	7.02	1,507.41	+H
Cyanidin 3-O-xyloside	419.09	419.09	1.59	3.79	7.56	1,618.00	−e, +H
Dihydroquercetin 3-O-hexoside	466.11	489.10	0.72	1.48	4.43	3,258.50	+Na
Ellagic acid	302.00	303.01	0.37	1.23	5.69	119,562.75	+H, −e, +Na
Ellagic acid arabinoside	434.04	435.05	0.19	0.43	5.39	9,050.23	+H, +Na
Ellagic acid glucoside	464.05	465.06	1.43	3.08	4.27	4,554.70	+H, +Na
Epigallocatechin (−)	306.07	307.08	0.91	2.98	1.13	2,386.10	+H, +Na
Gallagic acid	604.01	604.00	−2.72	−4.50	4.17	1,057.14	−e
Gallic acid	170.02	171.02	0.23	1.37	0.96	2,218.83	+H
Isopeonidin 3-O-sambubioside	595.16	618.15	−3.60	−5.83	6.50	2,121.97	+Na, −H, −e
Kaempferol 3-(2G-rhamnosylrutinoside)	448.10	471.09	0.42	0.89	6.49	22,420.06	+Na, +H
Kaempferol 3-O-rhamnoside	432.10	433.11	0.44	1.00	6.48	2,342.33	+H, +Na
Leucopelargonidin	290.07	291.08	0.43	1.47	2.35	1,743.90	+H
Methylgalangin	286.04	287.05	0.50	1.74	6.49	15,837.07	+H
Punicalin	782.06	783.06	1.39	1.77	4.38	2,813.12	+H

Abbreviations: ESI, electrospray ionization; LC, Liquid chromatography; MS, mass spectrometer; PPE, pomegranate peel extract.

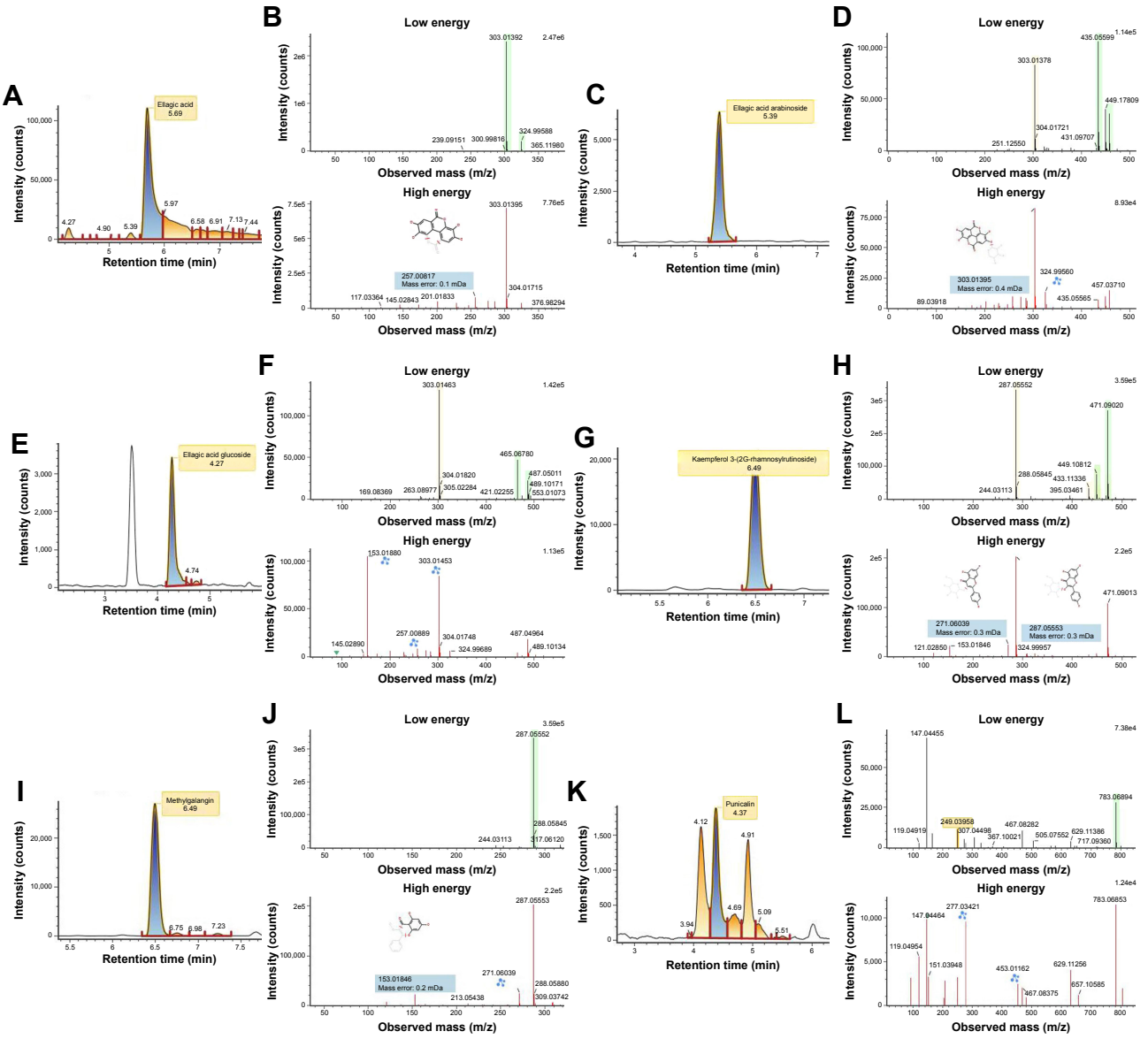

Figure 2 Representative liquid chromatography ion chromatogram and product ion mass spectra for (**A**, **B**) ellagic acid, (**C**, **D**) ellagic acid arabinoside, (**E**, **F**) ellagic acid glucoside, (**G**, **H**) kaempferol 3-(2G-rhamnosylrutinoside), (**I**, **J**) methylgalangin, (**K**, **L**) punicalin.

at room temperature (Figure 3D–F). The FTIR spectrum of AuNP yielded bands at 667.45, 698.45, 951.98, 1,021.19, 1,312.17, 1,409.90, 1,434.60, 1,661.32, 2,914.36, 2,998.50, and 3,444.58 cm^{-1} (Figure 3M). From the figures, a successful chemical conjugation was evident since the characteristic peak was observed at 3,444.58 cm^{-1}. This peak was related to the stretching vibration of O–H associated with flavonoids, terpene, and other polyphenols. On the other hand, the strong absorption peak at 1,661.32 cm^{-1} could be attributed to C=O (carbonyls) stretches from the PPE extract. The heavy bands at 2,914.36 and 2,998.50 cm^{-1} (seen in Figure 3M) and similar peaks at 2,914.36 and 2,998.50 cm^{-1} (seen in Figure 3M) corresponded to the medium alkyl C–H stretching vibrations, while the peak at 1,310.08 cm^{-1} (Figure 2M) and 1,312.17 cm^{-1} (Figure 2M) indicated a symmetrical medium (N–O) nitro compound stretching. The absorbance peaks at 1,044.76 cm^{-1} (Figure 3M) and 1,021.19 cm^{-1} (Figure 3M) demonstrated the variable covalent C–O stretch. These peaks did not interfere with the synthesis of the nanoparticles during the initial phase. Similarly, the medium carboxylic bends were observed in the absorbance range of 910–980 cm^{-1}. The absorbance peaks that ranged between 850 and 550 cm^{-1} and 690 and 515 cm^{-1} signified the simultaneous presence of alkyl chloride and alkyl bromide, both in PPE and PPE-AuNP. The peaks noted before and after the synthesis of PPE-mediated AuNP indicated that PPE might play an important

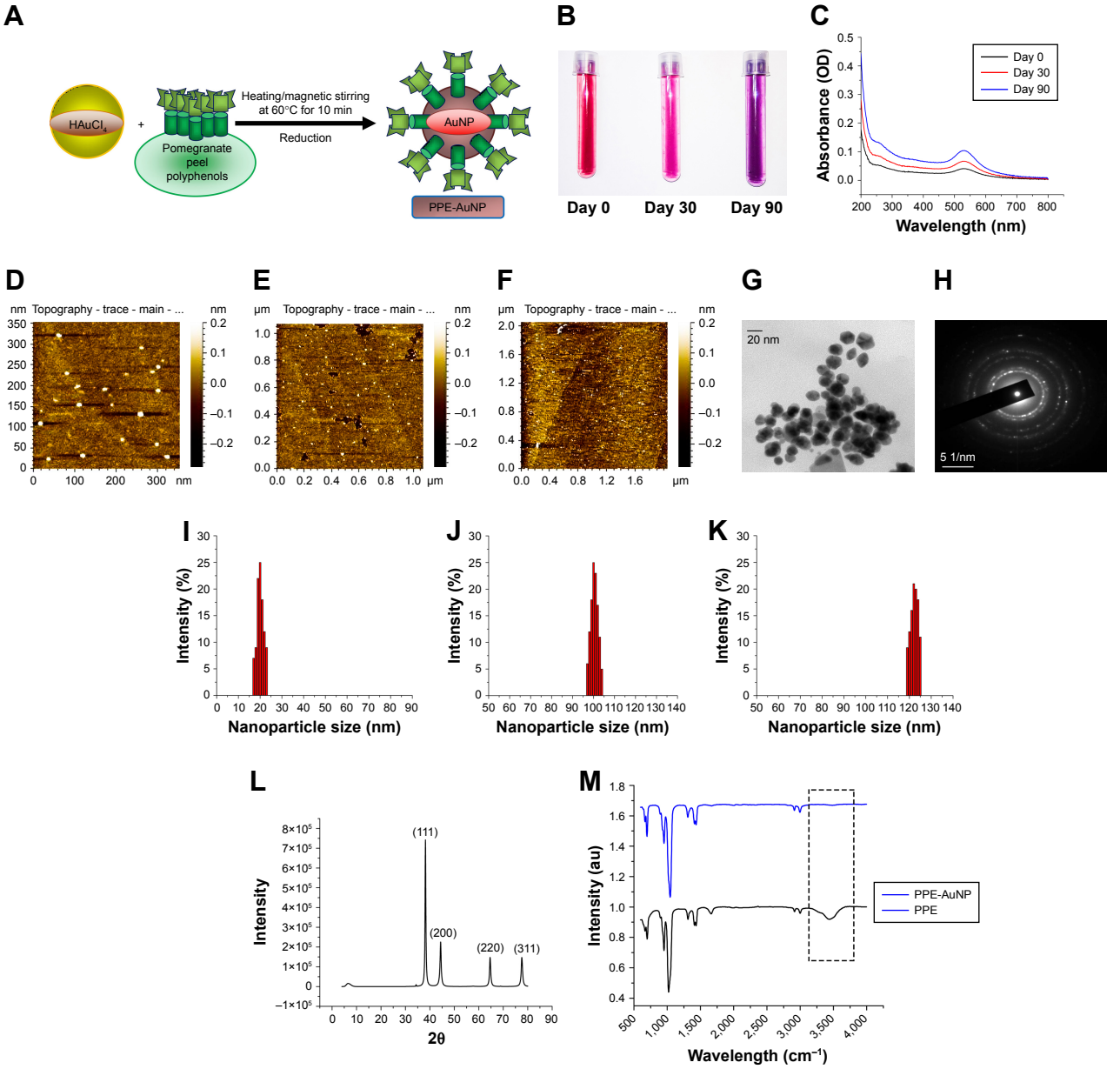

Figure 3 (**A**) Schematic representation of AuNP synthesis using PPE. (**B**) Representative photograph showing the color change of PPE-AuNP on room temperature storage (0, 30, and 90 days). (**C**) UV-visible spectra of PPE-AuNP dispersed in PBS on 0, 30, and 90-day storage. (**D**–**F**) Representative AFM micrographs of PPE-AuNP on 0, 30, and 90-day storage. (**G**, **H**) Representative TEM image and SAED pattern. (**I**–**K**) DLS analysis of PPE-AuNP (0, 30, and 90-day storage). (**L**) XRD pattern of PPE-AuNP. (**M**) FTIR spectra for PPE-AuNP and PPE alone.

Abbreviations: AFM, atomic force microscopy; AuNP, gold nanoparticle; FTIR, Fourier transform infrared; PPE, pomegranate peel extract; SAED, selected area of electron diffraction; TEM, transmission electron microscopy; UV, ultraviolet; XRD, X-ray diffraction.

role in stabilizing AuNPs through surface adsorption on bioreduced AuNP.

For the further confirmation of the crystalline nature of PPE-AuNP, XRD study was performed. The diffractograms are presented in Figure 3L. An intensive diffraction peak was observed at 2θ=38.2° corresponding to the (111) lattice plane of face-centered cubic (FCC) of Au. In addition, the detected diffraction peaks at 2θ=44.4°, 64.6°, and 78.2° corresponded to (200, 220) and (311) lattice planes of Au. But, the last three diffraction peaks were quite weaker than the previous one. A pictorial observation using a TEM established that the intensity of the diffraction peak of the (111) plane in PPE-AuNP was higher than other samples, which could possibly be attributed to the high population of polygonal AuNPs as established (Figure 3G and H). The size and morphology were further observed by HR-TEM. An FCC-like structure with size <20 nm was also observed. To confirm the phenomenon, the selected area of electron diffraction pattern

was documented (Figure 3H). The micrograph showed that the diffraction is composed of rings that were accompanied by dots corresponding to (111, 200, 220) and (311) planes.

PPE-AuNP restored STZ-induced reduction of body weight

A growing body of evidence suggested that a significant loss in body weight is accompanied with the STZ treatment. To evaluate the modulatory action of PPE-AuNP upon the STZ-induced loss, a specific modulation of the body weight was observed after 3 days of its initial application, followed by an assessment of average 3 days up to 18th day. A considerable reduction in body weight was noted in the animals with respect to the control. The initial average body weight after the STZ treatment was 18 g on the seventh day, which reduced to the final weight of 12 g at the end of experimental period (18th day). Compared to the STZ-treated group, a dose-dependent application of PPE-AuNP (5, 15, and 25 mg/kg) greatly restored the body weight. On the culminating day of our experiment (18th day), a significant restoration of the body weight (22 g) in the mice was achieved with the application of 25 mg/kg of PPE-AuNP (Figure 4A).

PPE-AuNP suppressed STZ-induced hyperglycemia

In order to assess the anti-diabetogenic potential of PPE-AuNP on STZ-induced hyperglycemic condition, fasting blood glucose along with the plasma insulin concentration was measured (Figure 4C and F). The STZ application considerably ($P<0.05$) enhanced the fasting blood glucose level.

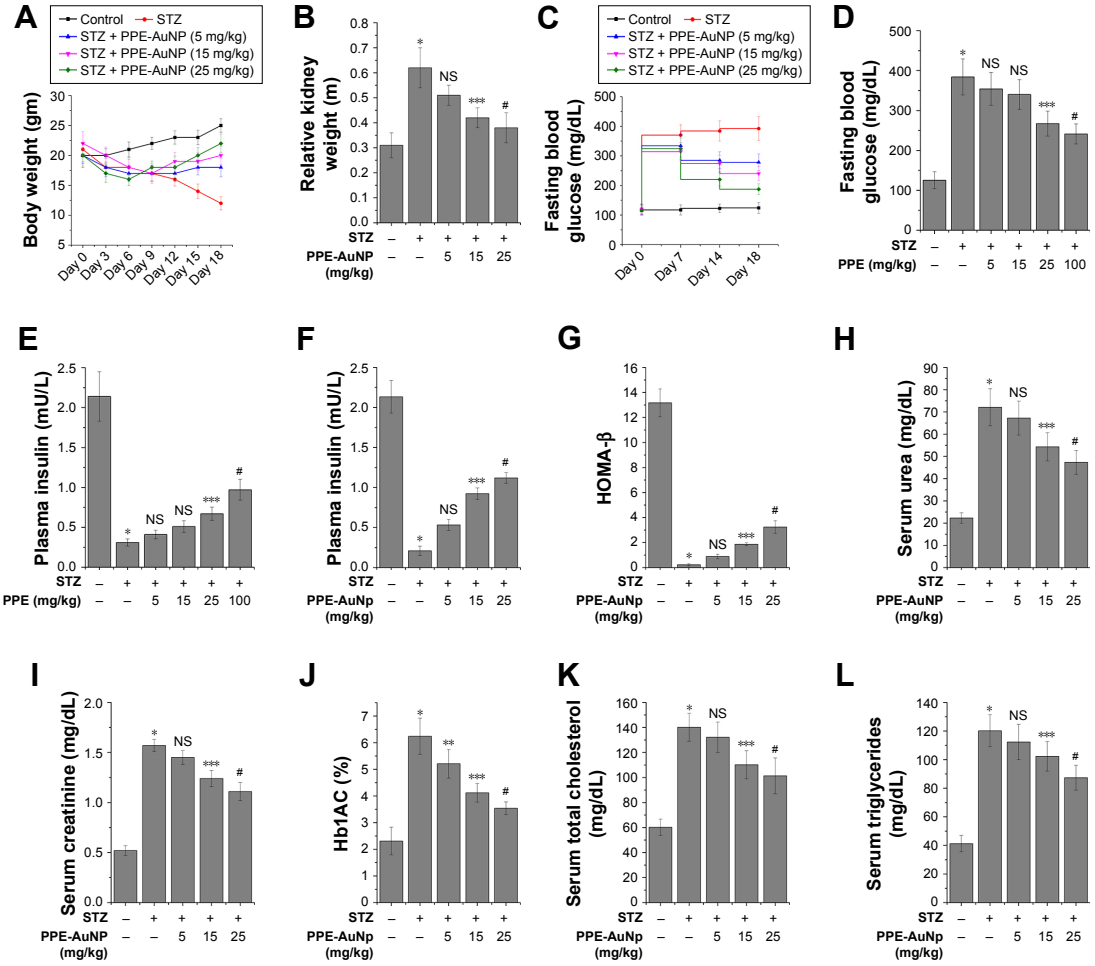

Figure 4 Representative bar graph showing (**A**) body weight changes, (**B**) kidney index, (**C**) level of fasting blood glucose, (**D**) level of fasting blood glucose upon the treatment of STZ along with PPE alone (5, 15, 25, and 100 mg/kg), (**E**, **F**) plasma insulin concentration upon the treatment of STZ along with/without of PPE alone and PPE-AuNP, (**G**) HOMA-β scoring, level of (**H**) serum urea, (**I**) serum creatinine, (**J**) %Hb1AC, level of (**K**) total cholesterol, and (**L**) triglyceride. Values are represented as mean ± SEM (n=6). $P<0.05$ was considered as significant. Statistical comparison: *Control vs STZ; **STZ vs STZ + PPE-AuNP (5 mg/kg); ***STZ vs STZ + PPE-AuNP (15 mg/kg); #STZ vs STZ + PPE-AuNP (25 mg/kg); NS refers to nonsignificant for STZ along with PPE-AuNP treatment. For STZ and PPE alone treatment, **control vs STZ; ***STZ vs STZ + PPE (25 mg/kg); #STZ vs STZ + PPE (100 mg/kg).

Abbreviations: AuNP, gold nanoparticle; HOMA, homeostatic model assessment; NS, nonsignificant; PPE, pomegranate peel extract; SEM, standard error of mean; STZ, streptozotocin.

Furthermore, a reduction of plasma insulin (0.10-fold) was observed. Whereas, when compared with the STZ-induced hyperglycemic condition, the use of PPE-AuNP markedly reduced the fasting blood glucose level (Figure 4C). Again, when PPE-AuNP was applied in a dose-dependent manner (5, 15, and 25 mg/kg), the reduction of plasma insulin was gradually normalized (0.25-, 0.43-, and 0.53-fold, respectively) (Figure 4F). Contrastingly, native PPE application in a dose-dependent manner (5, 15, 25, and 100 mg/kg) neither could reduce fasting blood glucose nor enhance plasma insulin over the STZ treatment (Figure 4D and E). This indicates that PPE-AuNP had better efficacy than native PPE to restore the function of pancreatic β cells, along with insulin secretion (Figure 4C–F).

When the pancreatic β-cell function was further evaluated by homeostatic model assessment (HOMA)-β assessment (Figure 4G), the STZ treatment markedly ($P<0.05$) reduced (0.02-fold) the HOMA-β score with respect to the control group. With the application of PPE-AuNP in a dose-dependent manner (5, 15, and 25 mg/kg), a gradual increase (0.07-, 0.14-, and 0.25-fold, respectively) in β-cell function was observed.

On the other hand, with the same treatment, an enhanced kidney weight (2.0-fold) was observed. Contrastingly, the application of PPE-AuNP in a dose-dependent manner (5, 15, and 25 mg/kg) significantly ($P<0.05$) reduced (1.7-, 1.4-, and 1.3-fold) the enhancement (Figure 4B).

PPE-AuNP suppressed STZ-induced renal toxicity

Previous reports suggested that STZ-treatment could impair kidney function by augmenting renal toxicity. To determine how the modulatory potential of PPE-AuNP could lower renal toxicity, two crucial renal function indices, namely serum urea and creatinine, were biochemically measured. As compared to the control group, elevated levels of serum urea (3.24-fold) and creatinine (2.94-fold) were found upon STZ treatment. In contrast, when we compared the STZ-induced hyperglycemic condition, a gradual application of PPE-AuNP ($P<0.05$) reduced the enhanced level of serum urea (3.01-, 2.47-, and 1.98-fold, respectively) and creatinine (2.68-, 2.34-, and 2.15-fold, respectively) (Figure 4H and I).

PPE-AuNP suppressed STZ-induced formation of glycated hemoglobin

While evaluating the potential efficacy of PPE-AuNP on hemoglobin glycation, STZ significantly ($P<0.05$) augmented the glycated hemoglobin (HbA1C) level (2.57-fold) compared with the control group (Figure 4J) in an STZ-induced hyperglycemic condition. However, the level of HbA1C was gradually reduced (2.12-, 1.72-, and 1.45-fold, respectively) in a dose-dependent manner (5, 15, and 25 mg/kg) with the treatment of PPE-AuNP.

PPE-AuNP reduced STZ-induced elevation of serum TC and TGs

With respect to the control group, in the STZ-induced hyperglycemic mice, considerable higher ($P<0.05$) levels of serum cholesterol (TC) (2.33-fold) and TG (3.0-fold) were observed (Figure 4K and L). Contrastingly, the levels of TC and TG were progressively reduced (2.22-, 1.82-, and 1.68-fold for TC; 2.75-, 2.53-, and 2.25-fold for TG) with a gradual dose (5, 15, and 25 mg/kg, respectively) of PPE-AuNP (Figure 4K and L).

PPE-AuNP suppressed STZ-induced iROS generation in nephritic tissue

As shown in Figure 5A and B, the STZ treatment considerably ($P<0.05$) enhanced (3.35-fold) the generation of iROS (an increased DCF fluorescence intensity) over the control group. As opposed, the PPE-AuNP treatment (5, 15, and 25 mg/kg) gradually reduced the iROS generation (by 2.51-, 2.18-, and 1.61-fold, respectively).

PPE-AuNP reduced STZ-mediated LPO in nephritic tissue

In the STZ-induced diabetic condition, LPO was enhanced, as depicted through enlarged TBARS (3.41-fold) in the studied nephritic tissue (Figure 5C). With the application of PPE-AuNP, the augmented level of renal TBARS was strikingly reduced in a dose-dependent manner (5, 15, and 25 mg/kg). As shown in Figure 5C, 15 mg/kg (1.86-fold) and 25 mg/kg (1.55-fold) of PPE-AuNP had significant ($P<0.05$) efficacious role in enhancing the endogenous antioxidants.

PPE-AuNP modulated STZ-induced enzymatic and non-enzymatic antioxidant in nephritic tissue

The assessment of the protective role of PPE-AuNP reflected a decline in ($P<0.05$) the SOD activity (0.13-fold) and also in the level (0.31-fold) of GSH level in the STZ-treated diabetic condition. Contrary to this was the treatment with PPE-AuNP administrated in a dose-dependent manner (5, 15, and 25 mg/kg), where a gradual restoration toward normalcy for both SOD (0.17-, 0.26-, and 0.71-fold, respectively) and for GSH (0.35-, 0.55-, and 0.63-fold, respectively) was noted (Figure 5D and E).

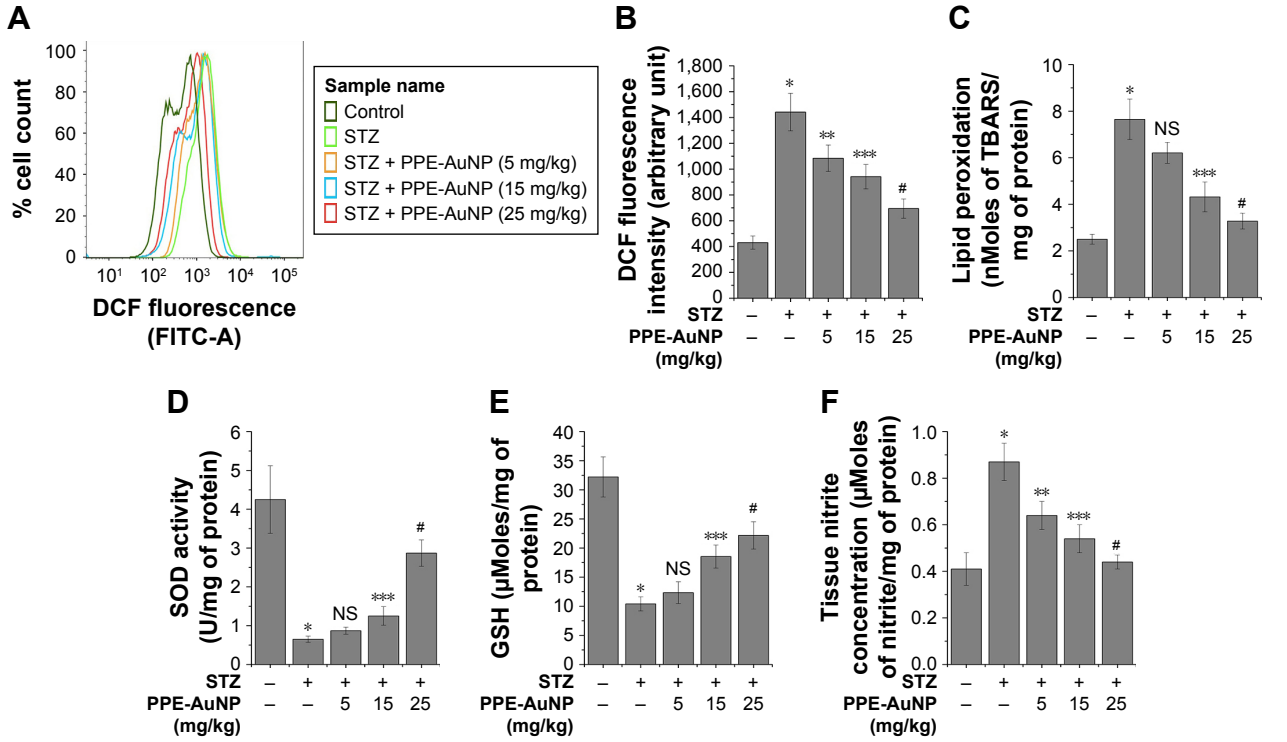

Figure 5 Modulatory role of PPE-AuNP in the alteration of STZ-induced oxidative stress indices. (**A**) Representative flow cytometric dot plot showing intercellular DCF fluorescence of the isolated renal cells. Cells were isolated from the respective murine kidney tissue after the completion of STZ and PPE-AuNP treatment. (**B**) Bar graph showing relative DCF fluorescence intensity of renal cells. Representative bar graphs showing (**C**) LPO, (**D**) SOD activity, (**E**) intercellular GSH, and (**F**) tissue nitrite formation. Values are represented as mean ± SEM (n=6). $P<0.05$ was considered as significant. Statistical comparison: *Control vs STZ; **STZ vs STZ + PPE-AuNP (5 mg/kg); ***STZ vs STZ + PPE-AuNP (15 mg/kg); #STZ vs STZ + PPE-AuNP (25 mg/kg).

Abbreviations: AuNP, gold nanoparticle; GDH, glutathione; LPO, lipid peroxidation; NS, nonsignificant; PPE, pomegranate peel extract; SEM, standard error of mean; SOD, superoxide dismutase; STZ, streptozotocin.

PPE-AuNP inhibited STZ-induced cellular nitrite formation in nephritic tissue

Cellular nitrite, the common denominators of DN, is associated with the initiation of various cellular anomalies in the renal system. As shown in Figure 5F, the augmented (2.18-fold) level of cellular nitrite markedly ($P<0.05$) reduced (1.53-, 1.35-, and 1.23-fold, respectively) with the application of PPE-AuNP (5, 15, and 25 mg/kg).

PPE-AuNP altered STZ-induced structural anomalies in nephritic tissue

A histological examination of the functional and pathological changes was carried out to investigate the therapeutic efficacy of PPE-AuNP in protecting the STZ-induced DN. Figure 6A revealed a typical architecture of nephritic tissue, such as an average glomerular size along with the basement membrane in the control group (as observed on hematoxylin and eosin staining). A marked degree of vacuolar degeneration in nephritic tubules along with the thickened basement membrane and widened podocyte membrane was recorded in the STZ-treated condition. As opposed, PPE-AuNP significantly reduced the vacuolar degeneration of nephritic tubules, causing a reduction in the thickened basement membrane in the STZ-treated diabetic state. This confirmed the altered nephritic injury index (Figure 6B). In addition, Figure 6A demonstrates severe glycogen and collagen deposition, the essential indices of glomerular sclerosis, around the glomerulus of nephritic tissue treated with STZ (Figure 6C) and tubulointerstitial fibrosis (Figure 6D). However, with PPE-AuNP (5, 15, and 25 mg/kg), the distinct accumulation of both was restored as observed in the suppressed level of glomerular sclerosis and tubulointerstitial score.

PPE-AuNP reduced STZ-induced renal fibrosis

DN is often associated with renal fibrosis, a particular state of excessive accumulation of extracellular matrix, where fibrogenic factor such as TGF-β, and Collagen IV are excessively accumulated. In order to confirm the association of STZ-induced DN with renal fibrosis and also determine the defensive role of PPE-AuNP in preventing the state, immunofluorescence was carried out to assess the expression of

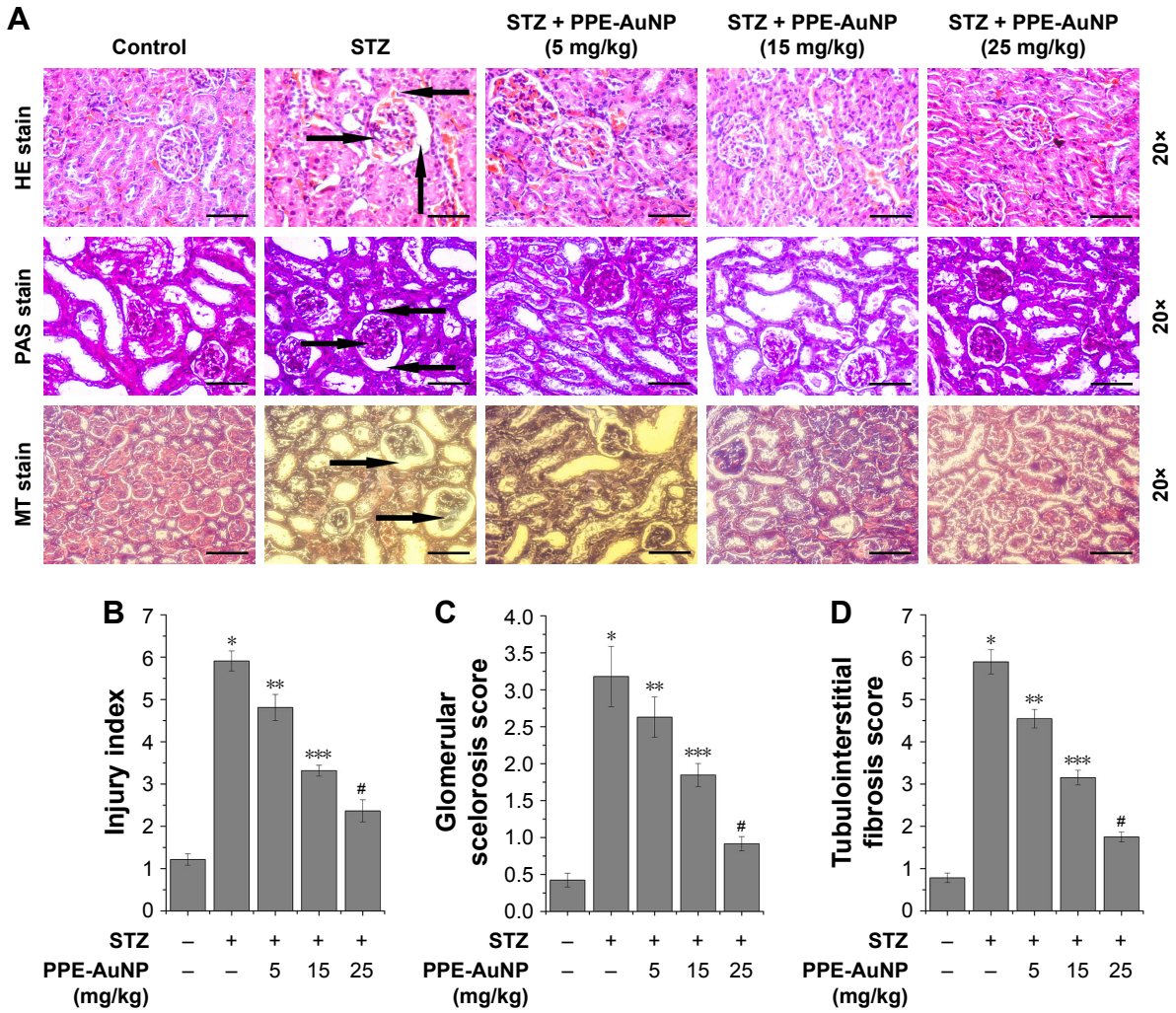

Figure 6 Renal tissue morphological assessment by histopathology using (**A**) hematoxylin and eosin staining, periodic acid–Schiff staining, Masson's trichrome staining (magnification: 20×); the arrows highlight morphological change. Representative bar graph showing quantitative analysis of (**B**) nephritic injury index, (**C**) glomerular sclerosis score, and (**D**) tubulointerstitial fibrosis. Values are represented as mean ± SEM (n=6). $P<0.05$ was considered as significant. Statistical comparison: *Control vs STZ; **STZ vs STZ + PPE-AuNP (5 mg/kg); ***STZ vs STZ + PPE-AuNP (15 mg/kg); #STZ vs STZ + PPE-AuNP (25 mg/kg).

Abbreviations: AuNP, gold nanoparticle; H&E, hematoxylin and eosin; MT, Masson's trichrome; NS, nonsignificant; PAS, periodic acid-Schiff; PPE, pomegranate peel extract; SEM, standard error of mean; STZ, streptozotocin.

TGF-β as well as collagen IV. Figure 7 revealed that STZ significantly enhanced TGF-β and collagen IV expression, as evident in relative fluorescence intensities of FITC and PE, respectively. But, there was a gradual decline of TGF-β and collagen IV with the dose-dependent treatment of PPE-AuNP (5, 15, and 25 mg/kg).

PPE-AuNP reduced STZ-induced AGE-RAGE activation in nephritic tissue

Numerous reports demonstrated that an elevated level of blood glucose could glycate endogenous proteins to produce AGEs through a non-enzymatic process. This is known to bind to the specific RAGE, following the activation of signaling cascade-associated with the DN. In order to determine the role of PPE-AuNP in protein glycation and associated signaling system in the hyperglycemic state, flow cytometry was used to assess the expression of AGE and its receptor, RAGE (Figure 8A–D). In the STZ-treated condition, an augmented ($P<0.05$) expression of both AGE (2.72-fold) and RAGE (3.83-fold) was observed. But, the treatment of PPE-AuNP (5, 15, and 25 mg/kg) dramatically suppressed both of them (1.66-, 1.31-, and 1.04-fold, respectively, for AGE as well as 2.92-, 2.88-, and 1.68-fold, respectively, for RAGE) (Figure 8A–D).

PPE-AuNP suppressed STZ-induced NOX4 and p-p47 activation in nephritic tissue

Scientific evidences have suggested that AGE-RAGE coupling triggers the activation downstream signaling system,

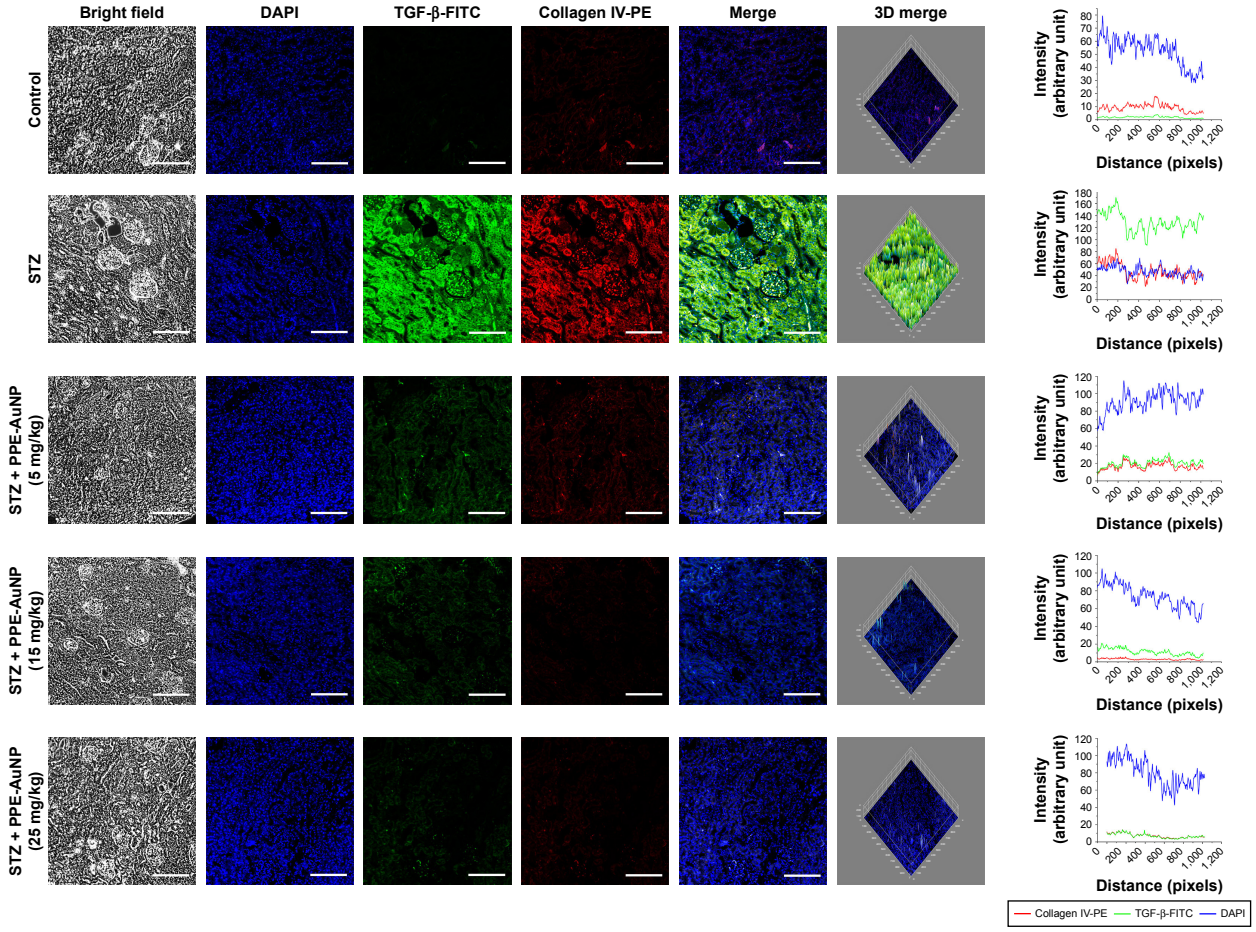

Figure 7 Immunofluorescence images demonstrating the expression of TGF-β and collagen IV. Slides were viewed using a confocal microscope (magnification 20×). Respective fluorescence intensities (TGF-β-FITC, collagen IV-PE, and DAPI) were analyzed using ImageJ software through RGB calculator.
Abbreviations: PE, phycoerythrin; PPE-AuNP, pomegranate peel extract-stabilized gold nanoparticle; RGB, red-green-blue; STZ, streptozotocin; TGF-β, transforming growth factor β.

especially NADPH oxidase (NOX family of protein) that leads to the generation of ROS. In order to determine the effect of PPE-AuNP in the STZ-induced activation of NOX and to evaluate the correlation between AGE-RAGE and ROS generation in STZ-induced condition, the expression level of NOX family protein, namely NOX4 and $p47^{phox}$, was measured using flow cytometry (Figure 8E–H). STZ significantly ($P<0.05$) increased the expression of NOX4 (4.42-fold) and the phosphorylation of $p47^{phox}$ (4.92-fold) over the control group. However, with the application of PPE-AuNP in a dose-dependent (5, 15, and 25 mg/kg) manner, the augmented appearance as well as the phosphorylation was reduced (3.25-, 2.89-, and 1.64-fold, respectively, for NOX4, while 4.37-, 3.14-, and 2.58-fold, respectively, for $p47^{phox}$) (Figure 8E–H).

PPE-AuNP inhibited STZ-induced MAPK pathway activation in nephritic tissue

To investigate the direct involvement of ROS in the activation of MAPK in hyperglycemic condition and to evaluate the ameliorative role of PPE-AuNP in the modulation of STZ-induced MAPK activation, the expression level of ERK1/2 and p38 module of MAPK was assessed through immunoblotting (Figure 9A–D). When compared to the control group, the STZ-treatment markedly ($P<0.05$) increased the phosphorylation of Raf1 (3.24-fold), ERK1/2 (2.98-fold), p38 (1.58-fold), and its upstream regulator, TAK1 (2.24-fold). On the other hand, the PPE-AuNP treatment (5, 15, and 25 mg/kg) gradually diminished the STZ-induced phosphorylation of the Raf1 (2.12-, 2.01-, and 1.22-fold, respectively), ERK1/2 (2.04-, 1.88-, and 1.45-fold, respectively), p38 (1.45-, 1.12-, and 0.97-fold, respectively), and TAK1 (2.14-, 1.98-, and 1.68-fold respectively) with respect to the group that was treated with STZ alone (Figure 9A–D).

PPE-AuNP reduced STZ-induced NF-κB pathway activation in nephritic tissue

NF-κB, a crucial redox-assisted transcription factor, is involved in the regulation of inflammation associated with

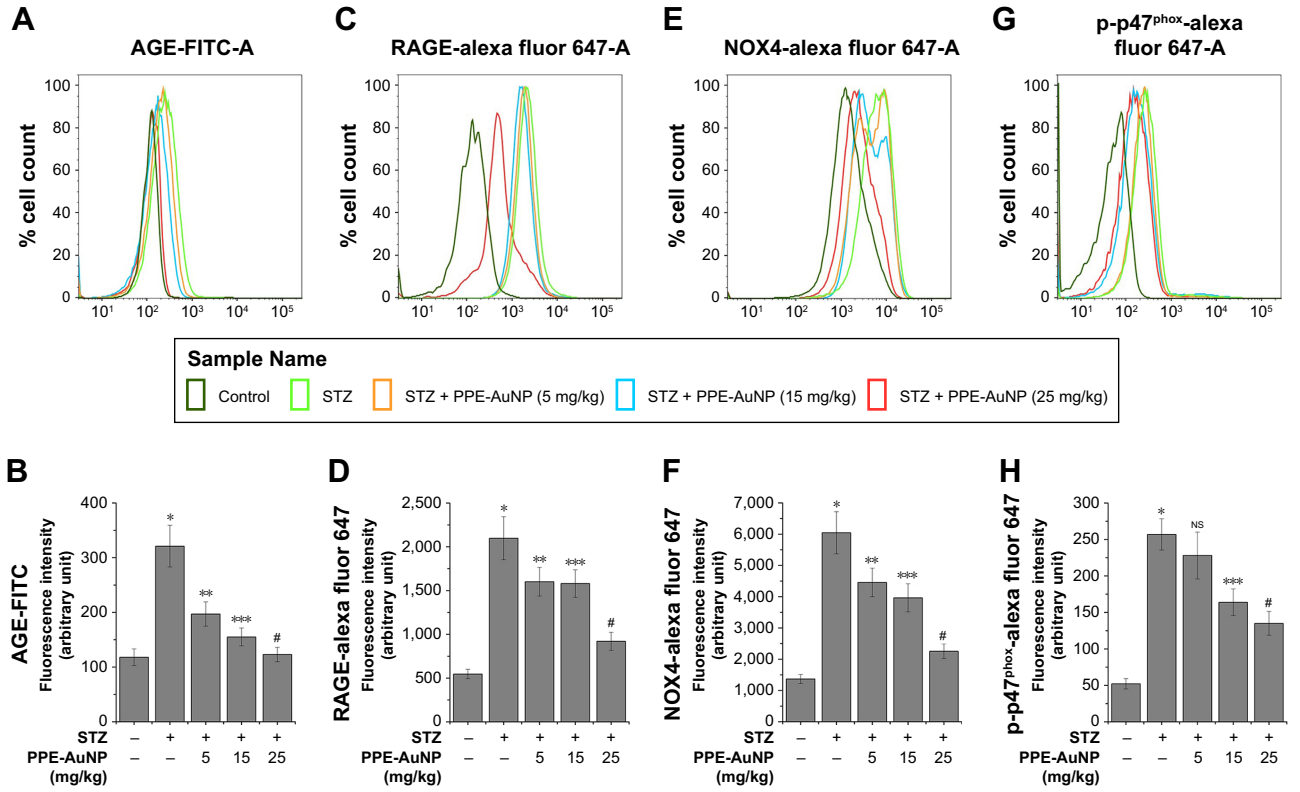

Figure 8 Representative flow cytometric histogram showing (**A**) AGE, (**C**) RAGE, (**E**) NOX-4, and (**G**) p-p47^{Phox} expression.
Notes: (**B**–**H**) Bar graph showing relative fluorescence intensities of AGE-FITC, RAGE-AF647, NOX4-AF647, and p-p47^{Phox}-AF647, respectively. Values are represented as mean ± SEM (n=6). $P<0.05$ was considered as significant. Statistical comparison: *Control vs STZ; **STZ vs STZ + PPE-AuNP (5 mg/kg); ***STZ vs STZ + PPE-AuNP (15 mg/kg); #STZ vs STZ + PPE-AuNP (25 mg/kg).
Abbreviations: AGE, advanced glycated end product; AuNP, gold nanoparticle; NS, nonsignificant; PPE, pomegranate peel extract; RAGE, receptor for advanced glycated end product; SEM, standard error of mean; STZ, streptozotocin.

hyperglycemia through the modulation of MAPK pathway. To investigate the modulatory role of PPE-AuNP in regulating the STZ-mediated activation of the NF-κB pathway, immunoblot analysis was carried out to evaluate the phosphorylation of NF-κB pathway components. Figure 9E revealed a pronounced phosphorylation ($P<0.05$) of IKKα/β (1.76-fold) and IκBα (2.14-fold) in nephritic tissue when treated with STZ. This suggested that STZ could activate NF-κB as p-IKKα/β, which could further phosphorylate IκBα, followed by the activation of the NF-κB subunit by withdrawing the inhibitory action. Interestingly, it also elevated ($P<0.05$) the phosphorylation of NF-κB subunit, p65 (2.24-fold), and p50 (2.74-fold) over the control group. On the other hand, compared with the STZ-treated group alone in a dose-dependent manner (5, 15, and 25 mg/kg), the PPE-AuNP treatment suppressed the augmented phosphorylation of IKKα/β (1.53-, 1.11-, and 1.05-fold, respectively), IκBα (2.01-, 1.68-, and 1.38-fold, respectively), p65 (1.84-, 1.74-, and 1.34-fold, respectively), and p50 (2.25-, 1.88-, and 1.56-fold, respectively) (Figure 9E and F).

Furthermore, STZ could activate and trigger the nuclear translocation of p65 as observed in the increased relative fluorescence intensity of PE. However, when treated with PPE-AuNP in a graded dose (5, 15, and 25 mg/kg), a moderate to severe reduction of PE fluorescence intensity in terms of p65 expression was also found (Figure 10).

PPE-AuNP inhibited STZ-induced STAT3 phosphorylation

When performing the immunoblot analysis, the STZ treatment noticeably augmented STAT3 phosphorylation (2.1-fold) in nephritic tissue, indicating the activation of pro-inflammatory state in excessive hyperglycemia. On the contrary, a low to moderate change in dephosphorylation of STAT3 (1.87-, 1.54-, and 1.32-fold, respectively) was also evident upon the PPE-AuNP treatment (5, 15, and 25 mg/kg) (Figure 9E and F).

PPE-AuNP reduced STZ-induced pro-inflammatory burden in nephritic tissue

NF-κB is involved in the regulation of numerous pro-inflammatory cytokines, namely IL-1β, interferon γ, IL-6, IL-10, and TNF-α. With the application of STZ, an enhanced

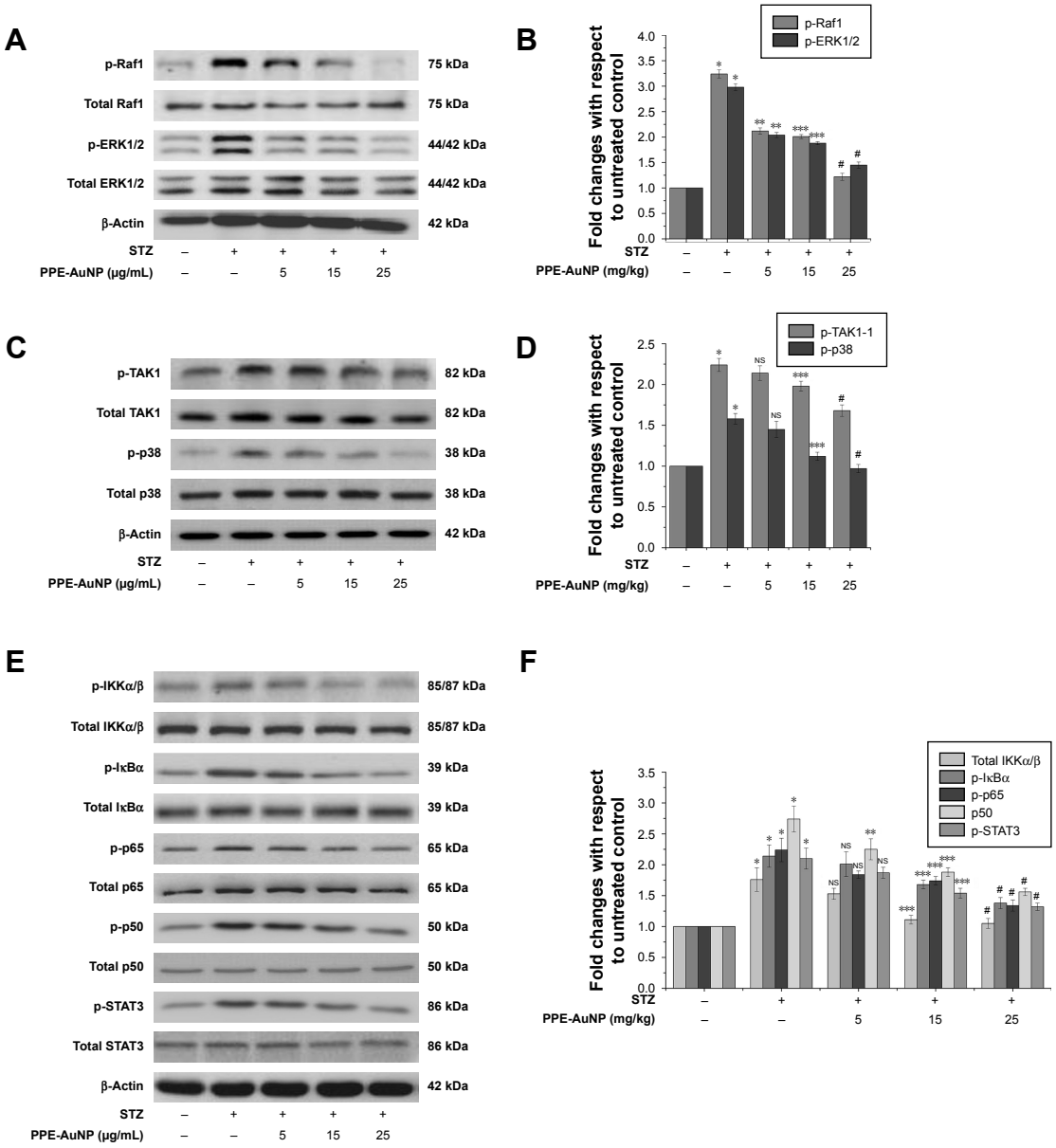

Figure 9 Modulatory role of PPE-AuNP on STZ-induced MAPK-guided NF-κB/STAT3 pathway activation in renal tissue. (**A**, **C**, **E**) Representative immunoblots of p-Raf1, total Raf1, p-ERK1/2, total ERK1/2, p-TAK1, total TAK1, p-p38, total p38, p-IKKα/β, total IKKα/β, p-IκBα, total IκBα, p-p65, total p65, p-p50, total p50, p-STAT3, and total STAT3. (**B**, **D**, **F**) Densitometric analysis of relative protein expression of p-Raf1, total Raf1, p-ERK1/2, total ERK1/2, p-TAK1, total TAK1, p-p38, total p38, p-IKKα/β, total IKKα/β, p-IκBα, total IκBα, p-p65, total p65, p-p50, total p50, p-STAT3, and total STAT3. β-Actin was served as internal control. Values are presented as mean ± SEM (n=6). $P<0.05$ was considered as significant. Statistical comparison: *Control vs STZ; **STZ vs STZ + PPE-AuNP (5 mg/kg); ***STZ vs STZ + PPE-AuNP (15 mg/kg); #STZ vs STZ + PPE-AuNP (25 mg/kg).

Abbreviations: AuNP, gold nanoparticle; NS, nonsignificant; PPE, pomegranate peel extract; SEM, standard error of mean; STZ, streptozotocin.

($P<0.05$) level of pro-inflammatory cytokines was evident in nephritic tissue, but dropped down with PPE-AuNP (5, 15, and 25 mg/kg) (Table 2).

As observed in an enhanced relative fluorescence intensity of APC, STZ also increased the COX2 expression in renal tissues. Contrastingly, the PPE-AuNP treatment (5, 15, and 25 mg/kg) gradually decreased the relative fluorescence intensity of APC, indicating the dose-dependent reduction in the COX2 expression (Figure 11).

PPE-AuNP modulated STZ-induced alteration of the Nrf2 pathway in nephritic tissue

Nuclear factor (erythroid-derived 2)-like 2 (Nrf2) is another essential redox-regulated transcription factor, which is involved in the regulation of endogenous antioxidant response in addition to the Phase-II detoxifying enzyme expression. To evaluate the involvement of PPE-AuNP in the management

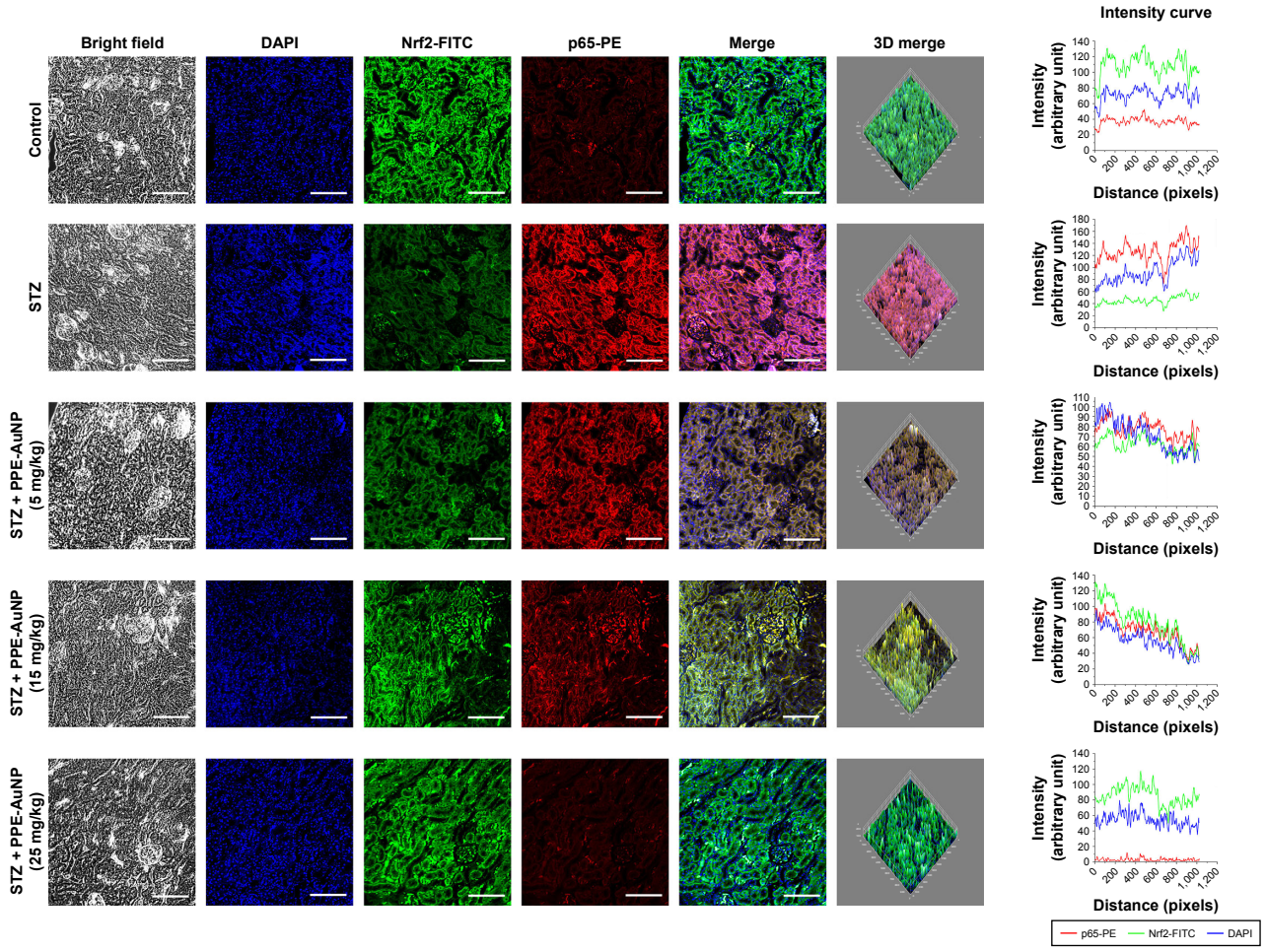

Figure 10 Immunofluorescence images demonstrating the expression of Nrf2 and NF-κB (p65). Slides were viewed using a confocal microscope (magnification 20×). Respective fluorescence intensities (Nrf2-FITC, p65-PE, and DAPI) were analyzed using ImageJ software through RGB calculator.
Abbreviations: PE, phycoerythrin; RGB, red-green-blue.

of endogenous antioxidants in the STZ-treated condition, flow cytometry and confocal microscopy were used to determine the expression of the Nrf2 pathway components. Figure 12E–H reveals that STZ notably ($P<0.05$) upregulated the expression of Keap1 (3.69-fold), masking the Nrf2 activation through its inhibitory action. As evident in the relative fluorescence intensity of FITC, this also suppressed the phosphorylation of Nrf2 (0.23-fold).

A similar result was also observed in the immunofluorescence analysis, where a significant expression of Nrf2 was

Table 2 The level of cytokines in the serum measured after the completion of experimentation using ELISA

Group	IL-1β (pg/mL)	IFNγ (pg/mL)	IL-6 (pg/mL)	IL-10 (pg/mL)	TNF-α (pg/mL)
Control	22.34±4.21	6.21±0.74	4.55±0.63	80.24±9.27	14.21±2.14
STZ	78.24±8.24*	47.25±5.24*	47.35±6.24*	142.21±17.24*	38.24±4.25*
STZ + PPE-AuNP (5 mg/kg)	70.54±9.35^{NS}	40.21±5.17^{NS}	41.25±5.21^{NS}	132.14±14.31**	30.14±3.47**
STZ + PPE-AuNP (15 mg/kg)	54.21±6.21***	31.21±4.78***	34.24±3.14***	120.24±13.21***	21.21±3.74***
STZ + PPE-AuNP (25 mg/kg)	47.24±5.24$^{\#}$	24.21±3.85$^{\#}$	27.35±2.47$^{\#}$	112.37±12.34$^{\#}$	17.25±2.14$^{\#}$

Notes: Values are represented as mean ± SEM (n=6). $P<0.05$ was considered as significant. Statistical comparison: *Control vs STZ; **STZ vs STZ + PPE-AuNP (5 mg/kg); ***STZ vs STZ + PPE-AuNP (15 mg/kg); $^{\#}$STZ vs STZ + PPE-AuNP (25 mg/kg).
Abbreviations: AuNP, gold nanoparticle; IFNγ, interferon γ; NS, nonsignificant; PPE, pomegranate peel extract; SEM, standard error of mean; STZ, streptozotocin; TNF-α, tumor necrosis factor-alpha.

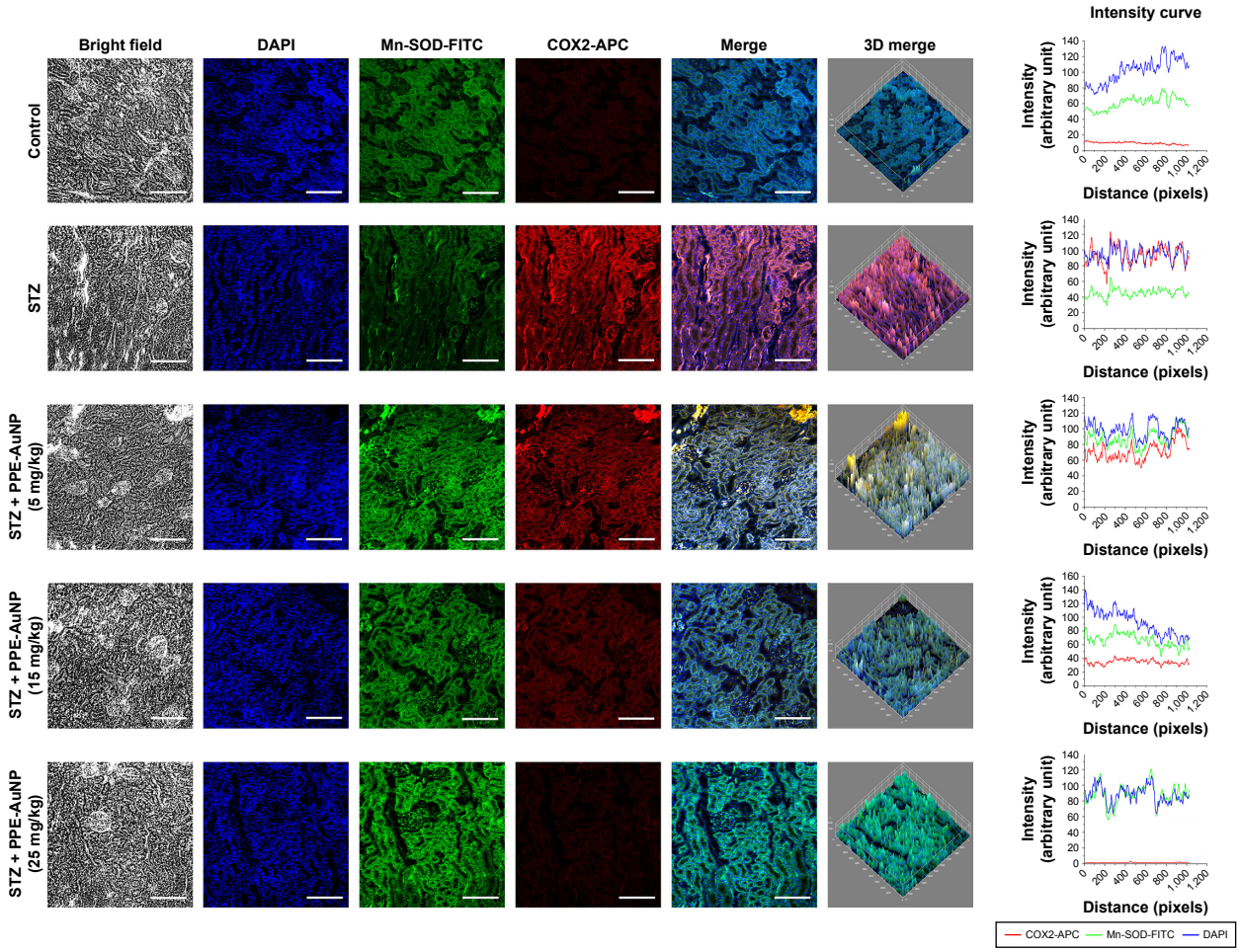

Figure 11 Immunofluorescence images demonstrating the expression of Mn-SOD and COX2. Slides were viewed using a confocal microscope (magnification 20×). Respective fluorescence intensities (Mn-SOD-FITC, COX2-APC, and DAPI) were analyzed using ImageJ software through RGB calculator.
Abbreviations: APC, allophycocyanin; RGB, red-green-blue; SOD, superoxide dismutase.

evident in the nephritic tissue treated with STZ. By contrast, the application of PPE-AuNP in a dose-dependent manner (5, 15, and 25 mg/kg) gradually reduced the expression of Keap1 (1.88-, 1.84-, and 1.33-fold, respectively), followed by the enhancement of phosphorylation of Nrf2 (0.46-, 0.72-, and 0.82-fold, respectively). This was also confirmed in immunofluorescence analysis, where the PPE-AuNP treatment enhanced the Nrf2 localization in nephritic tissues (Figure 10).

PPE-AuNP regulated STZ-induced modulation of PI3K/AKT pathway in nephritic tissue

PI3K/AKT pathway is known to control Nrf2 activation by suppressing the Keap1 activity. The diminished phosphorylation of PI3K (Tyr 458) (0.23-fold) and AKT (Ser 473) (0.14-fold) was observed in the STZ treatment of the control group. However, the suppressed expression of PI3K (0.55-, 0.61-, and 0.66-fold, respectively) and AKT (0.23-, 0.42-, and 0.68-fold, respectively) was gradually phosphorylated as well as activated upon the treatment of PPE-AuNP (5, 15, and 25 mg/kg), as evident in the relative fluorescence intensity of FITC (Figure 12A–D).

PPE-AuNP reversed STZ-induced inhibition of Mn-SOD expression in renal tissue

Researchers have demonstrated that mitochondrial-superoxide dismutase (Mn-SOD), an endogenous mitochondrial enzyme, is regulated by Nrf2-assisted mechanism and also involved in the regulation of antioxidant response. In order to evaluate the protective efficacy of PPE-AuNP in the homeostatic balance of antioxidant response in the STZ-mediated hyperglycemic state, Mn-SOD expression was assessed by immunofluorescence. Figure 11 demonstrates that the STZ treatment notably suppressed Mn-SOD expression in renal tissues

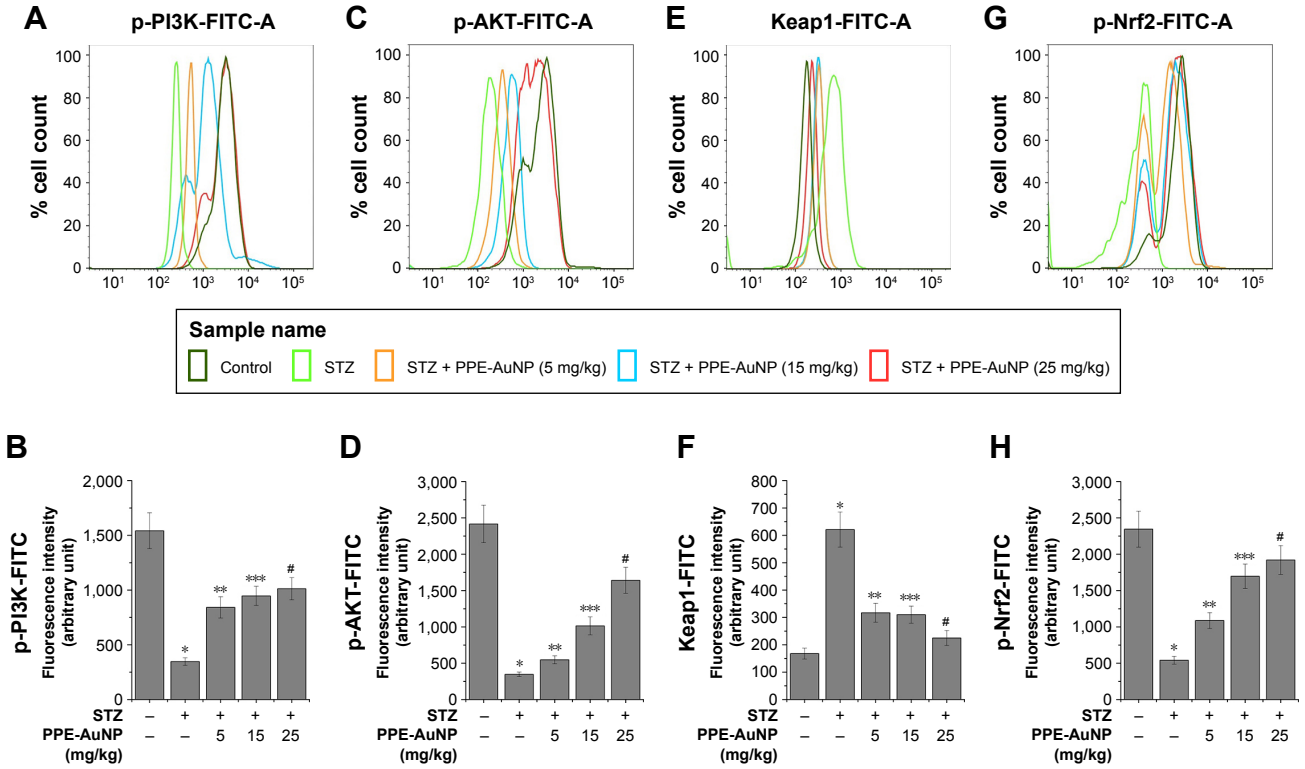

Figure 12 Representative flow cytometric histogram showing (**A**) p-PI3K, (**C**) p-AKT, (**E**) Keap1 and (**G**) p-Nrf2 expression. (**B**, **D**, **F**, **H**) Bar graph showing relative fluorescence intensities of p-PI3K-FITC, p-AKT-FITC, Keap1-FITC, and p-Nrf2-FITC, respectively. Values are represented as mean ± SEM (n=6). $P<0.05$ was considered as significant. Statistical comparison: *Control vs STZ; **STZ vs STZ + PPE-AuNP (5 mg/kg); ***STZ vs STZ + PPE-AuNP (15 mg/kg); #STZ vs STZ + PPE-AuNP (25 mg/kg).
Abbreviations: AuNP, gold nanoparticle; NS, nonsignificant; PPE, pomegranate peel extract; SEM, standard error of mean; STZ, streptozotocin.

when compared with the control group. However, the reduced level of Mn-SOD expression was gradually increased with the application of PPE-AuNP in a concentration-dependent manner (5, 15, and 25 mg/kg).

Bioavailability of PPE-AuNP

As shown in Figure 13A, a gradual increase in the plasma concentration of AuNP was noted with the application of PPE-AuNP (5, 15, and 25 mg/kg) on the 1st day, nevertheless, this reading was much lower on the final day of the experiment (10th day), suggesting a rapid clearance of AuNP from plasma to a different organ. Interestingly, the renal concentration of PPE-AuNP was increased on the 10th day of application, which indicated its retention in renal tissues throughout the experimental period (Figure 13B). The resultant accumulation and elimination of PPE-AuNP (1st and 10th day) were further estimated in hepatic, splenic, cardiac, and lung tissues. An increased accumulation of PPE-AuNP was found in the hepatic and cardiac tissues on the 1st day of treatment, while the accumulated concentration was markedly decreased on the 10th day (Figure 13C and E). In case of splenic and lung tissues, the accumulated concentration was increased sharply on the final day of experimentation (10th day), when treated with PPE-AuNP in a dose dependent manner (5, 15, and 25 mg/kg) (Figure 13D and F). The data revealed a homeostatic distribution in the PPE-AuNP concentration in plasma as well as other organs such as kidney, liver, spleen, heart, and lung.

Discussion

As mentioned earlier, DN has long been recognized as end-stage renal disorder worldwide, which might be attributed to severe hyperglycemia.[34] An elevated level of blood glucose can trigger the damage of renal cells as well as the tiny blood vessels of kidney, leading to nephropathy.[35] The current therapeutic approach of DN remains poor, and most of the medical interventions are incapable of reversing or even delaying the disease progression. In this regard, nanomedicine, especially gold nanostructure, has recently been used for the treatment of diabetic complications due to its higher bioavailability and its modulatory potential on hyperglycemia-induced redox-regulated cellular signaling mechanism.[36]

The methanolic fraction of PPE was used as a reducing agent as well as a stabilizer in the green synthesis of AuNP.

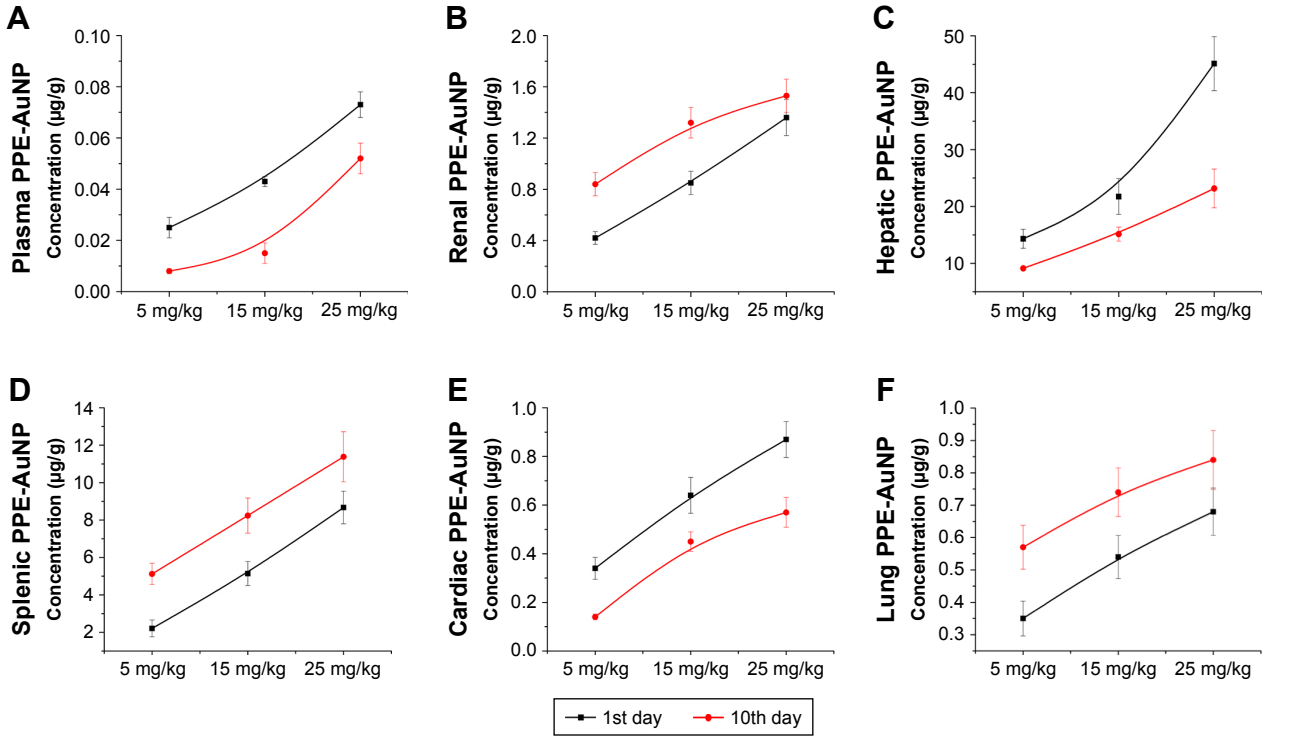

Figure 13 The concentration of AuNP in (**A**) plasma, (**B**) renal tissue, (**C**) hepatic tissue, (**D**) splenic tissue, (**E**) cardiac tissue, and (**F**) lung tissue after the single application of PPE-AuNP in 0 day and 10th day. Values are represented as mean ± SEM (n=6).
Abbreviations: AuNP, gold nanoparticle; PPE, pomegranate peel extract; SEM, standard error of mean.

The phenolic compounds of PPE, especially ellagic acid and its derivatives, reduced Au^{3+} to Au^{0} and stabilized the AuNP through surface interactions with C=O and −OH groups of phenols. The obtained PPE-AuNP was mostly round in shape with a mean diameter of 20 nm. It had optical spectra with a dominant plasmonic band centered at 525 nm, representing the typical signature of the dipolar plasmon resonance of individual spherical AuNP. The mean hydrodynamic diameter of 20.4 nm confirmed the presence of an additional stabilizing layer around the particles. The AuNP synthesis was conducted in various concentrations of PPE to determine the optimum level for reducing and stabilizing AuNP. The higher the concentration of PPE, the more intense was the color of the generated colloid. However, at a higher concentration of PPE, the AuNP core had a faster growth, causing an increase in the frequency of collisions of nanoparticles to form agglomeration. The optimum concentration of PPE was 0.01% (w/v), which was enough to reduce all Au^{3+}. As mentioned earlier, the resultant PPE-AuNP was stable at 4°C for 6 months. However, at room temperature, the stability was reduced to 30 days. This reflected the formation of agglomeration due to the condensed collision on prolonged preservation.

As a glucosamine-nitrosourea compound, STZ has substantial toxicity against pancreatic β-cells, resulting in the reduction of blood insulin and the elevation of blood glucose. It has been commonly used for inducing diabetes in the experimental animal because of its high reproducibility and low cost.[37] As evident in the current study, the STZ treatment (60 mg/kg body weight) exhibited the pathophysiological characteristics of DM, including an increase in blood glucose, a reduction in plasma insulin, and an elevation of serum creatinine and serum urea. After 18 days, a striking reduction in the body weight corresponding to hyperglycemia was noted. The relative kidney weight, fasting blood glucose, serum urea, and serum creatinine were found to be higher in hyperglycemic condition, while plasma insulin level and HOMA-β scoring were lower. By contrast, when the animals were treated with PPE-AuNP in different concentration (5, 15, and 25 mg/kg body weight) for 5 alternate days, it suppressed the fasting blood glucose level, followed by an alteration in renal toxicity indices, serum urea, and serum creatinine. This finding clearly suggests the ameliorative role on the STZ-induced renal dysfunction. On the one hand, PPE-AuNP also enhanced the plasma insulin level, thereby restoring the HOMA-β scoring. This in turn hints at the pancreoprotective efficacy. On the other hand, PPE-AuNP reversed the hyperglycemia-induced renal hypertrophy, as evident in the reduction of relative kidney weight, and a

substantial change in the body weight at the end of the experiment, implicating the renoprotective efficiency.

Apart from irregular glucose metabolism, dyslipidemia is involved in exacerbating DN through the modulation of multiple cellular signaling systems related to lipid metabolism. A few reports have also shown that hyperlipidemia, one of the critical risk factors for DN, is associated with the glomerular injury.[38] In many instances, hyperglycemia is directly associated with hyperlipidemia which can promote renal damage.[38] In the STZ treatment, the elevated levels of TC and serum TG were found, but were markedly reduced with the treatment of PPE-AuNP in a dose-dependent manner. This indicates that PPE-AuNP could improve the lipid accumulation in a hyperglycemic condition and, therefore, decrease the risk of microvascular disease and related complications.

A vast degree of glomerular lesions and the thickening of the basement membrane observed in the diabetic condition, coupled with the fibrous tissue accumulation as well as matrix degradation, led to glomerular sclerosis and tubulointerstitial fibrosis.[35] However, PPE-AuNP considerably suppressed the accumulation of fibrous tissues and restored the hyperglycemia-induced renal morphological change. This established the fact that PPE-AuNP could slow down the progression of renal damage in diabetic condition. Studies have also suggested that a direct involvement exists between renal fibrosis and TGF-β and collagen IV expression. Both TGF-β and collagen IV play an imperative role in pathological processes during the development and progression of DN. These factors regulate ECM remodeling leading to structural alteration, mesangial expansion, and tubular dysfunction.[39] The enhanced expressions of TGF-β and collagen IV were found in the diabetic condition which further confirmed the tubulointerstitial fibrosis. Interestingly, it was shown that PPE-AuNP treatment significantly diminished the expressions of TGF-β and collagen IV. This indicates its probable involvement in suppressing glomerular sclerosis and tubulointerstitial fibrosis in hyperglycemic condition.

Oxidative stress, another essential aspect in hyperglycemia-induced DN, plays a principal role in the etiology of numerous diabetic complications.[5] In our study, an increased level of renal lipid peroxide along with the imbalance of endogenous antioxidant enzymes reflected the disturbance of cellular milieu in severe hyperglycemic condition, finally leading to the renal nephropathy. On the contrary, the enhanced level of ROS also supported the consequences of oxidative stress upon the STZ treatment. As suggested in previous reports regarding the antioxidant nature of various nanoparticles,[40] PPE-AuNP could reduce ROS generation, followed by lipid peroxide formation in diabetic condition. It could also increase the diminished level of endogenous renal antioxidants, which indicates that PPE-AuNP can act as a potent exogenous antioxidant.

The enhanced level of free blood glucose can react with endogenous protein to form AGE, which can couple with a specific receptor, RAGE, followed by the activation of downstream mediators. AGEs are accountable for the thickening the ECM, and often, implicating in renal dysfunction. Also, the long biological half-life of AGE is responsible for the continuous reaction with free glucose to form a more glycated product. This results in the alteration of protein structure and makes ECM more resistant to degradation processes through the accumulation of cross-linked products in renal cells.[41] A growing body of evidence has shown that activation of RAGE triggers NADPH oxidase (NOX) families of proteins, which can activate ROS generation through the radical conversion of molecular oxygen (O_2). The whole process of redox reaction has vital relevance in the development of DN.[41] The current study demonstrated that PPE-AuNP could suppress the hyperglycemia-induced protein glycation by inhibiting the hyperactivation of RAGE-guided NOX-4/$p47^{phox}$ activation, followed by the inhibition of the ROS generation.

A growing body of literature has supported that concomitant activation of MAPK module, p38-MAPK as well as ERK1/2 appears to be one of the critical factors in the pathophysiology of DN.[42] The resultant hyperphosphorylation of MAPK in diabetic condition is regulated by ROS which can modulate the activation of crucial redox-assisted transcription factors, NF-κB and STAT3, leading to renal inflammation.[43] The result demonstrated that the STZ-induced ROS significantly augmented the phosphorylated form of MAPK, including Raf1, Tak1, p38, and ERK1/2. Whereas, because the hyperphosphorylated state of MAPK module was further dephosphorylated with the application of PPE-AuNP in a dose-dependent manner (5, 15, and 25 mg/kg body weight), it suggests that PPE-AuNP could regulate the MAPK activation through the suppression of ROS.

One of the essential redox-regulated transcription factors, NF-κB, is also activated in diabetic condition. Numerous reports have revealed that hyperglycemia-induced DN and associated inflammation are guided upon NF-κB while most of the pro-inflammatory cytokines are transcriptionally regulated through NF-κB.[44] In a basal condition, NF-κB is sequestered in the cytoplasm through the inhibitory action of IκB. Upon activation by stressors, such as ROS, and the upstream modulators, MAPK, the IKK subunits, especially,

IKKα/β is phosphorylated. Finally, the phosphorylated form of IKKα/β in turn phosphorylates IκB leading to its proteasomal degradation and leaving the inhibitory action on NF-κB subunits, p65 and p50. The activated and phosphorylated form of p65 and p50 subunit is then translocated toward the nucleus which regulates the plethora of pro-inflammatory cytokines, including TGF-β, IL-6, TNF-α, and IL-1β.[45] The hyperphosphorylation of IKKα/β, as well as IκBα and p65/p50 that was found with the STZ treatment confirmed the previous reports that DN is dependent on NF-κB activation. However, PPE-AuNP-mediated dephosphorylation of NF-κB subunits, along with its modulators in hyperglycemic condition, suggests the inhibitory role of PPE-AuNP in reducing the proinflammatory cytokine burden in DN as it could markedly suppress the critical proinflammatory cytokines.

Nrf2, an essential transcription factor, is involved in the modulation of endogenous antioxidant response.[46] Earlier studies showed that pomegranate polyphenols might directly activate Nrf2, or indirectly through the modulation of the upstream regulator, PI3K/AKT.[47–49] Commonly,

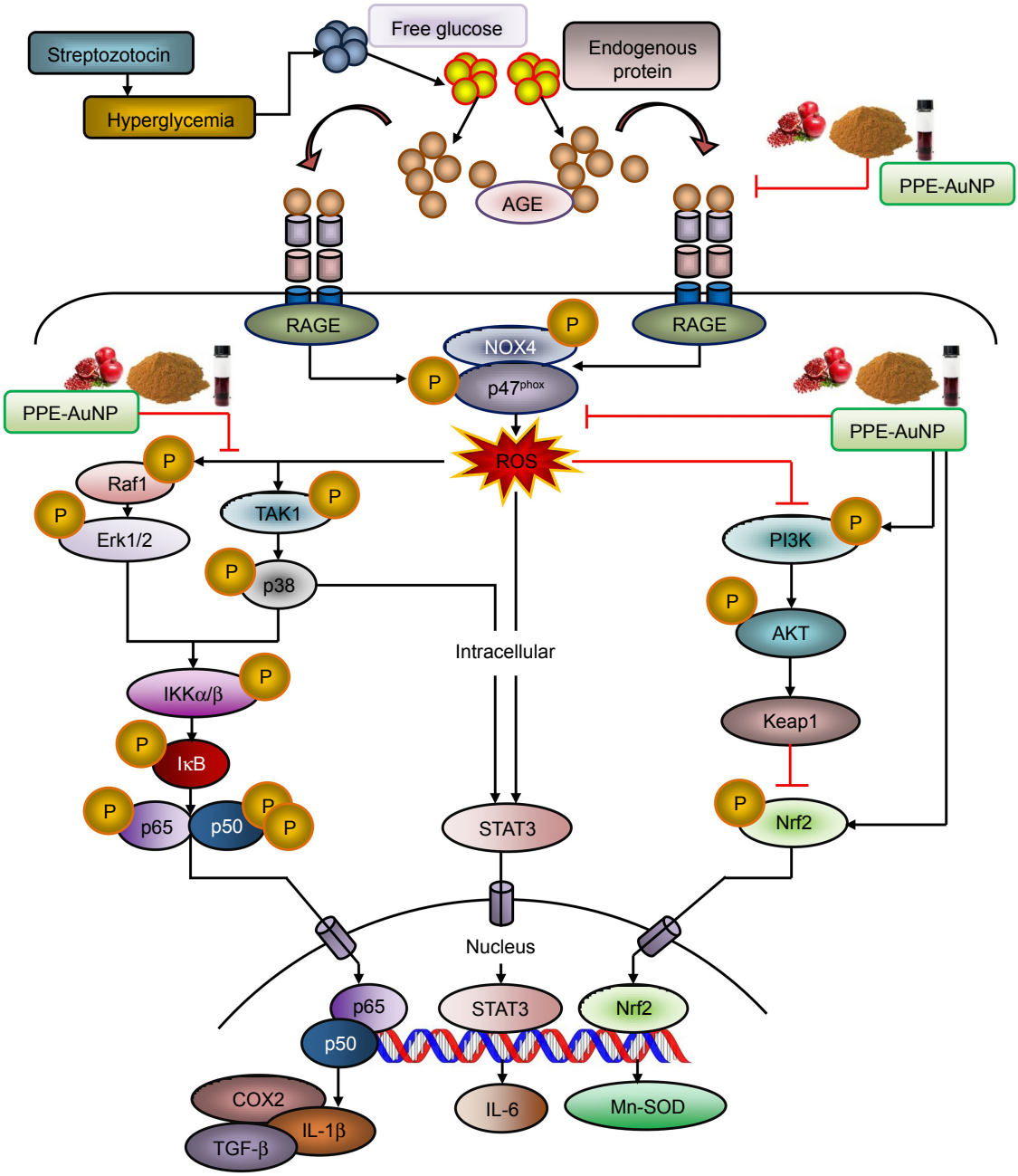

Figure 14 Graphical representation illustrating the probable mechanism of action of PPE-AuNP in ameliorating STZ-induced diabetic nephropathy.
Abbreviations: AuNP, gold nanoparticle; PPE, pomegranate peel extract; STZ, streptozotocin.

Nrf2 is inactivated in the cytoplasm by the masking effect of the negative regulator, Keap1. In response to the dietary phytochemicals, Keap1 can be inactivated, but the nuclear translocation of Nrf2 activated. The free form of Nrf2 is then capable of entering in the nucleus where it binds to the specific antioxidant responsive element (ARE) of the plethora of cytoprotective genes, including Mn-SOD, HO-1, and NQO1.[46] STZ-induced ROS, on the one hand, markedly diminished the phosphorylation of PI3K/AKT, while it could enhance the activation of Keap1 and reduce the activity of Nrf2. On the other hand, a dose-dependent treatment of PPE-AuNP reversed the inhibitory consequences of cytoprotection. The enhanced phosphorylation of PI3K/AKT and Nrf2 suggests the possible role of PPE-AuNP in activating Nrf2-guided cytoprotective system. Upon the PPE-AuNP treatment, the observed augmented expression of Mn-SOD and reduced expression of Keap1 confirmed renoprotection in the studied animals. Some recent results have suggested that a crosstalking mechanism exists between NF-κB and Nrf2, whereas Nrf2 deficiency enhances NF-κB-guided proinflammation.[7,50] On the other hand, as NF-κB subunit, p65 is physically associated with Keap1, thus providing an additional mechanism of Nrf2-ARE inhibition. In our study, PPE-AuNP activated Nrf2 and inhibited NF-κB, which enabled the presence of crosstalk mechanism between these two transcription factors in DN.

Throughout the experimental period, PPE-AuNP accumulation in renal, splenic, and lung tissues gradually increased in a dose-dependent manner, while the plasma, hepatic, and cardiac concentrations of PPE-AuNP were progressively lowered, indicating stable retention of PPE polyphenols in renal tissue as well as splenic and lung tissues. This might reduce the hyperglycemia-induced progression of DN and associated inflammation.

Conclusion

In this paper, we have developed PPE-stabilized AuNP which exhibited significant efficacy for curing DN. The result demonstrated that the STZ treatment distinctly augmented the loss of pancreatic β-cell function followed by an increase in free blood glucose level which enhanced protein glycation to produce AGE. Furthermore, STZ-mediated AGE could bind to the specific receptor, RAGE, which triggered ROS generation through NOX4/p47^{phox}-guided redox reaction. The marked activation of MAPK/NF-κB-regulated proinflammation and fibrous tissue accumulation was also evident in the hyperglycemic condition that turned on the STAT3. In contrast, PPE-AuNP was able to reverse the entire oxidative state by inhibiting protein glycation as well as scavenging the ROS, followed by the dephosphorylation of MAPK/NF-κB/STAT3-mediated proinflammatory burden. Also, the finding showed that PPE-AuNPs exhibited endogenous antioxidant response which maintained the renal homeostasis in DN (Figure 14). In summary, PPE-AuNP might be used as a prophylactic approach to diminish DN and also a signature component for the treatment of hyperglycemia-induced complications. These potential applications of PPE-AuNP in preventing oxidative stress and their adverse effects, induced at hyperglycemic conditions, have opened up the way for a new resource of cost economic alternative in the treatment of diabetic progression.

Acknowledgments

The research is supported by the National Medicinal Plant Board (NMPB), Ministry of Ayurveda, Yoga & Naturopathy, Unani, Siddha and Homoeopathy (AYUSH), Government of India. A research fellowship from University Grants Commission-Department of Atomic Energy (UGC-DAE), Government of India, to Mr Snehasis Mishra is gratefully acknowledged. The authors gratefully acknowledge Dr Suparna Banerjee for the improvement of English usage. In addition, the authors are also thankful to Mr Tanmoy Dalui, Mrs Debalina Chakraborty, Sri. Binayak Pal, and Smt. Banasri Das of Central Instrumentation Facility, Council of Scientific & Industrial Research–Indian Institute of Chemical Biology for providing flow cytometer and confocal microscope facilities. The authors are very obliged to Dr Asim Bhowmik for his guidance in some parts of this study.

Disclosure

The authors report no conflicts of interest in this work.

References

1. Greenhill C. New mechanism for insulin resistance. *Nat Rev Endocrinol*. 2016;12(5):249.
2. Brownlee M. The pathobiology of diabetic complications: a unifying mechanism. *Diabetes*. 2005;54(6):1615–1625.
3. Dabla PK. Renal function in diabetic nephropathy. *World J Diabetes*. 2010;1(2):48–56.
4. Adeshara KA, Diwan AG, Tupe RS. Diabetes and complications: cellular signaling pathways, current understanding and targeted therapies. *Curr Drug Targets*. 2016;17(11):1309–1328.
5. Manda G, Checherita AI, Comanescu MV, Hinescu ME. Redox signaling in diabetic nephropathy: hypertrophy versus death choices in mesangial cells and podocytes. *Mediators Inflamm*. 2015; 2015(6):1–13.
6. Kanwar YS, Sun L, Xie P, Liu FY, Chen S. A glimpse of various pathogenetic mechanisms of diabetic nephropathy. *Annu Rev Pathol*. 2011; 6:395–423.
7. Wardyn JD, Ponsford AH, Sanderson CM. Dissecting molecular cross-talk between Nrf2 and NF-κB response pathways. *Biochem Soc Trans*. 2015;43(4):621–626.

8. Ganesh Yerra V, Negi G, Sharma SS, Kumar A. Potential therapeutic effects of the simultaneous targeting of the Nrf2 and NF-κB pathways in diabetic neuropathy. *Redox Biol*. 2013;1(1):394–397.
9. Ly C, Yockell-Lelièvre J, Ferraro ZM, Arnason JT, Ferrier J, Gruslin A. The effects of dietary polyphenols on reproductive health and early development. *Hum Reprod Update*. 2015;21(2):228–248.
10. Zheng H, Whitman SA, Wu W, et al. Therapeutic potential of Nrf2 activators in streptozotocin-induced diabetic nephropathy. *Diabetes*. 2011;60(11):3055–3066.
11. Bahadoran Z, Mirmiran P, Azizi F. Dietary polyphenols as potential nutraceuticals in management of diabetes: a review. *J Diabetes Metab Disord*. 2013;12(1):43.
12. Bahmani M, Baharvand-Ahmadi B, Tajeddini P, Rafieian-Kopaei M, Naghdi N. Identification of medicinal plants for the treatment of kidney and urinary stones. *J Renal Inj Prev*. 2016;5(3):129–133.
13. Rafieian-kopaei M. Medicinal plants for renal injury prevention. *J Renal Inj Prev*. 2013;2(2):63–65.
14. Zarfeshany A, Asgary S, Javanmard SH. Potent health effects of pomegranate. *Adv Biomed Res*. 2014;3:100.
15. Ismail T, Sestili P, Akhtar S. Pomegranate peel and fruit extracts: a review of potential anti-inflammatory and anti-infective effects. *J Ethnopharmacol*. 2012;143(2):397–405.
16. Volf I, Ignat I, Neamtu M, Popa V. Thermal stability, antioxidant activity, and photo-oxidation of natural polyphenols. *Chem Pap*. 2014;68(1): 121–129.
17. Dash SS, Bag BG. Synthesis of gold nanoparticles using renewable Punica granatum juice and study of its catalytic activity. *Appl Nanosci*. 2014;4(1):55–59.
18. De Araújo RF, de Araújo AA, Pessoa JB, et al. Anti-inflammatory, analgesic and anti-tumor properties of gold nanoparticles. *Pharmacol Rep*. 2017;69(1):119–129.
19. Panichayupakaranant P, Itsuriya A, Sirikatitham A. Preparation method and stability of ellagic acid-rich pomegranate fruit peel extract. *Pharm Biol*. 2010;48(2):201–205.
20. Koley TK, Khan Z, Oulkar D, et al. High resolution LC-MS characterization of phenolic compounds and the evaluation of antioxidant properties of a tropical purple radish genotype. *Arabian J Chemistry*. 2017.
21. Elia P, Zach R, Hazan S, Kolusheva S, Porat Z, Zeiri Y. Green synthesis of gold nanoparticles using plant extracts as reducing agents. *Int J Nanomedicine*. 2014;9:4007–4021.
22. Ahmad A, Syed F, Shah A, et al. Silver and gold nanoparticles from Sargentodoxa cuneata: synthesis, characterization and antileishmanial activity. *RSC Adv*. 2015;5(90):73793–73806.
23. Pradhan A, Bepari M, Maity P, Roy SS, Roy S, Choudhury SM. Gold nanoparticles from indole-3-carbinol exhibit cytotoxic, genotoxic and antineoplastic effects through the induction of apoptosis. *RSC Adv*. 2016; 6(61):56435–56449.
24. Barham D, Trinder P. An improved colour reagent for the determination of blood glucose by the oxidase system. *Analyst*. 1972;97(151):142–145.
25. Manna K, Khan A, Kr das D, et al. Protective effect of coconut water concentrate and its active component shikimic acid against hydroperoxide mediated oxidative stress through suppression of NF-κB and activation of Nrf2 pathway. *J Ethnopharmacol*. 2014;155(1): 132–146.
26. Das K, Ghosh M. Structured DAG oil ameliorates renal injury in streptozotocin-induced diabetic rats through inhibition of NF-κB and activation of Nrf2 pathway. *Food Chem Toxicol*. 2017;100: 225–238.
27. Manna K, Khan A, Biswas S, et al. Naringin ameliorates radiation-induced hepatic damage through modulation of Nrf2 and NF-κB pathways. *RSC Adv*. 2016;6(27):23058–23073.
28. Moron M, Depierre J, Mannervik B. Levels of glutathione, glutathione reductase and glutathione S-transferase activities in rat lung and liver. *Biochim Biophys Acta*. 1979;582(1):67–78.
29. Hevel JM, White KA, Marletta MA. Purification of the inducible murine macrophage nitric oxide synthase. Identification as a flavoprotein. *J Biol Chem*. 1991;266(34):22789–22791.
30. Kesh SB, Sikder K, Manna K, et al. Promising role of ferulic acid, atorvastatin and their combination in ameliorating high fat diet-induced stress in mice. *Life Sci*. 2013;92(17–19):938–949.
31. Bhanja, P, Mishra, S, Manna, K, Mallick A, Das Saha K, Bhaumik A. Covalent Organic Framework Material Bearing Phloroglucinol Building Units as a Potent Anticancer Agent. *ACS Appl Mater Interfaces*. 2017;9(37):31411–31423.
32. Manna K, Das U, Das D, et al. Naringin inhibits gamma radiation-induced oxidative DNA damage and inflammation, by modulating p53 and NF-κB signaling pathways in murine splenocytes. *Free Radic Res*. 2015;49(4):422–439.
33. Yang L, Kuang H, Zhang W, Aguilar ZP, Wei H, Xu H. Comparisons of the biodistribution and toxicological examinations after repeated intravenous administration of silver and gold nanoparticles in mice. *Sci Rep*. 2017;7(1)3303.
34. Yuan CM, Nee R, Ceckowski KA, Knight KR, Abbott KC. Diabetic nephropathy as the cause of end-stage kidney disease reported on the medical evidence form CMS2728 at a single center. *Clin Kidney J*. 2017;49(2):sfw112–sfw262.
35. Qian Y, Feldman E, Pennathur S, Kretzler M, Brosius FC. From fibrosis to sclerosis: mechanisms of glomerulosclerosis in diabetic nephropathy. *Diabetes*. 2008;57(6):1439–1445.
36. Tong F, Liu S, Yan B, Li X, Ruan S, Yang S. Quercetin nanoparticle complex attenuated diabetic nephropathy via regulating the expression level of ICAM-1 on endothelium. *Int J Nanomedicine*. 2017;12:7799–7813.
37. Furman Bl. Streptozotocin-induced diabetic models in mice and rats. *Curr Protoc Pharmacol*. 2015;70:5(47):41–20.
38. Jia G, Di F, Wang Q, et al. Non-alcoholic fatty liver disease is a risk factor for the development of diabetic nephropathy in patients with type 2 diabetes mellitus. *PLoS One*. 2015;10(11):e0142808.
39. Umezono T, Toyoda M, Kato M, et al. Glomerular expression of CTGF, TGF-beta 1 and type IV collagen in diabetic nephropathy. *J Nephrol*. 2006;19(6):751–757.
40. Phull AR, Abbas Q, Ali A, et al. Antioxidant, cytotoxic and antimicrobial activities of green synthesized silver nanoparticles from crude extract of Bergenia ciliata. *Future J Pharm Sci*. 2016;2(1):31–36.
41. Ramasamy R, Yan SF, Schmidt AM. Receptor for AGE (RAGE): signaling mechanisms in the pathogenesis of diabetes and its complications. *Ann N Y Acad Sci*. 2011;1243(1):88–102.
42. Adhikary L, Chow F, Nikolic-Paterson DJ, et al. Abnormal p38 mitogen-activated protein kinase signalling in human and experimental diabetic nephropathy. *Diabetologia*. 2004;47(7):1210–1222.
43. Schulze-Osthoff K, Ferrari D, Riehemann K, Wesselborg S. Regulation of NF-kappa B activation by MAP kinase cascades. *Immunobiology*. 1997;198(1–3):35–49.
44. Kuhad A, Chopra K. Attenuation of diabetic nephropathy by tocotrienol: involvement of NFkB signaling pathway. *Life Sci*. 2009;84(9–10): 296–301.
45. Liu T, Zhang L, Joo D, Sun SC. NF-κB signaling in inflammation. *Signal Transduct Target Ther*. 2017;2:17023.
46. Nguyen T, Nioi P, Pickett CB. The Nrf2-antioxidant response element signaling pathway and its activation by oxidative stress. *J Biol Chem*. 2009;284(20):13291–13295.
47. Sun W, Yan C, Frost B, et al. Pomegranate extract decreases oxidative stress and alleviates mitochondrial impairment by activating AMPK-Nrf2 in hypothalamic paraventricular nucleus of spontaneously hypertensive rats. *Sci Rep*. 2016;6(1):34246.
48. Li X, Liu L, Pischetsrieder M. Pomegranate (*Punica granatum* L.) wine polyphenols affect Nrf2 activation and antioxidant enzyme expression in human neuroblastoma cells (SH-SY5Y). *J Funct Foods*. 2017;38(A):140–150.
49. Bishayee A, Bhatia D, Thoppil RJ, Darvesh AS, Nevo E, Lansky EP. Pomegranate-mediated chemoprevention of experimental hepatocarcinogenesis involves Nrf2-regulated antioxidant mechanisms. *Carcinogenesis*. 2011;32(6):888–896.
50. Li W, Khor TO, Xu C, et al. Activation of Nrf2-antioxidant signaling attenuates NFkappaB-inflammatory response and elicits apoptosis. *Biochem Pharmacol*. 2008;76(11):1485–1489.